

# Anionic Nanoplastic Contaminants Promote Parkinson's Disease-Associated $\alpha$ -Synuclein Aggregation

**Zhiyong Liu**

Duke University

**Arpine Sokratian**

Duke University

**Addison Duda**

Duke University

**Enquan Xu**

Duke University

**Christina Stanhope**

Duke University

**Amber Fu**

Duke University

**Samuel Strader**

Duke University

**Huizhong Li**

Duke University

**Yuan Yuan**

Duke University

**Benjamin Bobay**

Duke University

**Joana Sipe**

Duke University

**Ketty Bai**

Duke University

**Iben Lundgaard**

Lund University

**Na Liu**

Lund University

**Belinda Hernandez**

Duke University

**Catherine Bowes Rickman**

Duke University

**Sara Miller**

Duke University

**Andrew West** (✉ [andrew.west@duke.edu](mailto:andrew.west@duke.edu))

Duke University

---

## Research Article

**Keywords:** microplastics, neurodegeneration, protein aggregation

**Posted Date:** October 13th, 2023

**DOI:** <https://doi.org/10.21203/rs.3.rs-3439102/v1>

**License:** © ⓘ This work is licensed under a Creative Commons Attribution 4.0 International License.

[Read Full License](#)

---

# Anionic Nanoplastic Contaminants Promote Parkinson's Disease-Associated $\alpha$ -Synuclein Aggregation

Zhiyong Liu\*<sup>1</sup>, Arpine Sokratian\*<sup>1</sup>, Addison M. Duda<sup>2</sup>, Enquan Xu<sup>1</sup>, Christina Stanhope<sup>1</sup>, Amber Fu<sup>1</sup>, Samuel Strader<sup>1</sup>, Huizhong Li<sup>1</sup>, Yuan Yuan<sup>1</sup>, Benjamin G. Bobay<sup>2</sup>, Joana Sipe<sup>3</sup>, Ketty Bai<sup>1</sup>, Iben Lundgaard<sup>4,5</sup>, Na Liu<sup>4,5</sup>, Belinda Hernandez<sup>6</sup>, Catherine Bowes Rickman<sup>6</sup>, Sara E Miller<sup>7</sup>, Andrew B. West<sup>1, 8\*\*</sup>

<sup>1</sup>Duke Center for Neurodegeneration and Neurotherapeutics, Duke University, Durham, NC, USA

<sup>2</sup>Department of Chemistry, Duke University, Durham, NC, USA

<sup>3</sup>Department of Civil and Environmental Engineering, Duke University, Durham, NC, USA.

<sup>4</sup>Department of Experimental Medical Science, Lund University, Lund, Sweden

<sup>5</sup>Wallenberg Center for Molecular Medicine, Lund University, Lund, Sweden

<sup>6</sup>Department of Ophthalmology and Cell Biology, Duke University, Durham, NC, USA.

<sup>7</sup>Department of Pathology, Duke University, Durham, North Carolina, USA.

<sup>8</sup>Aligning Science Across Parkinson's (ASAP) Collaborative Research Network, Chevy Chase, MD

\*Authors contributed equally to this work.

\*\*Corresponding author. Tel: +1 919 684 1656; E-mail: Andrew.West@Duke.edu

**Short title:** Nanoplastics promote  $\alpha$ -synuclein aggregation.

**Teaser:** Small plastic particles stimulate Parkinson's disease-associated features in the brain.

## **Abstract**

Recent studies have identified increasing levels of nanoplastic pollution in the environment. Here we find that anionic nanoplastic contaminants potently precipitate the formation and propagation of  $\alpha$ -synuclein protein fibrils through a high-affinity interaction with the amphipathic and non-amyloid component (NAC) domains in  $\alpha$ -synuclein. Nanoplastics can internalize in neurons through clathrin-dependent endocytosis, causing a mild lysosomal impairment that slows the degradation of aggregated  $\alpha$ -synuclein. In mice, nanoplastics combine with  $\alpha$ -synuclein fibrils to exacerbate the spread of  $\alpha$ -synuclein pathology across interconnected vulnerable brain regions, including the strong induction of  $\alpha$ -synuclein inclusions in dopaminergic neurons in the substantia nigra. These results highlight a potential link for further exploration between nanoplastic pollution and  $\alpha$ -synuclein aggregation associated with Parkinson's disease and related dementias.

## Introduction

Increased plastic production and deposition of waste worldwide have resulted in microplastic contaminants in water and food supplies (1–3). Microplastics, defined as particles smaller than 5 mm in diameter, can also include smaller nanoplastics (less than 1  $\mu\text{m}$ ). Single-use polystyrene products, such as foam packing materials, cups, and cutlery, are largely responsible for widespread polystyrene waste that contributes to overall plastic pollution (4, 5). Negatively charged small plastic particles are found in marine environments as a presumed consequence of ultraviolet radiation exposures and plastic erosion (6).

In experimental studies, anionic polystyrene nanoplastics induce endothelial leakiness and potentially compromise the blood-brain barrier in mammals by intercalating with cadherin dimers (7). A recent study found that polystyrene plastic pollution, among a few other types of plastic, circulates in the blood of most adults tested (8). In that study, a pyrolysis mass spectrometry approach suggested the concentration of polystyrene ranged from  $\sim 1$  to over 4  $\mu\text{g}$  per mL in about a quarter of blood samples analyzed from healthy controls, though particle sizes of nanoplastics in the brain have not been determined. In models, polystyrene nanoplastics have been reported to accumulate in the brain and penetrate into the parenchyma (9–13). Acrylic latex microspheres (0.02–0.2  $\mu\text{m}$  in diameter), administered through intracranial injections, have been widely used as neural-retrograde trafficking tracers (14, 15). It is unclear whether other chemical forms of nanoplastics, including charged polystyrene, can be internalized and trafficked in neurons once these contaminants are inside the brain (13, 16). Nonetheless, nanoparticles could hijack parts of the endocytic trafficking pathway to potentially travel along different circuits in the brain (17).

Among the fastest growing neurological disorders in the world, Parkinson's disease (PD) and related dementias are pathologically defined by the accumulation of  $\alpha$ -synuclein protein in vulnerable neurons in the brain (18). Increased longevity, heritable factors, and prolonged exposure to environmental challenges of largely unknown origins are suspected as principal driving factors for disease risk and progression (19).  $\alpha$ -Synuclein is typically a low-molecular-weight protein, but in PD-affected tissues, electron microscopy studies show that fibril structures interact with damaged lipids from various organelles, such as lysosomes and mitochondria (20). *In vitro* studies show that some types of charged nanoparticles can inhibit  $\alpha$ -synuclein fibril nucleation and fibril-seeded elongation (21). Graphene nanoparticles (less than 100 nm in diameter) administered to neuronal cultures and mice in pre-formed  $\alpha$ -synuclein fibril-seeded

models attenuate  $\alpha$ -synuclein aggregation in neurons (22). Conversely, *in vitro* studies show that nanospheres composed of polyethylenimine-coated carboxyl-modified polystyrene nanoparticles can increase  $\alpha$ -synuclein nucleation (21). Other types of particle surfaces, such as silica or zirconium, have primary effects on  $\alpha$ -synuclein fibril elongation and are essential components of diagnostic  $\alpha$ -synuclein seeding assays used to detect aggregated  $\alpha$ -synuclein seeds in patient biofluids and tissues (23, 24).

With the rise of new types of nanoparticles in the environment, studies in model systems related to  $\alpha$ -synuclein pathobiology may provide insights into what types of nanoparticles to further explore as potential toxins in PD. Among different types of plastic pollutants, the increase in polystyrene nanoplastics in the environment from single-use plastics, recent detection of polystyrene contaminants in blood, and past reports of anionic polystyrene plastics disrupting and crossing the blood brain barrier, suggest polystyrene nanoplastics as a relevant type of particle to explore for interaction with  $\alpha$ -synuclein. Here we find that anionic polystyrene nanoplastics bind to  $\alpha$ -synuclein with low to subnanomolar affinity which rapidly promotes  $\alpha$ -synuclein fibril formation and fibril-seeded pathology in cultured neurons, as well as in dopaminergic neurons in the intact wild-type mouse brain. Both  $\alpha$ -synuclein fibrils and nanoplastic particles internalize in neurons in a clathrin-dependent manner and converge at the lysosome where new  $\alpha$ -synuclein inclusions form. Although a rare occurrence in mice, direct nanoplastic exposure, by itself, can result in the *de novo* formation of mature phosphorylated  $\alpha$ -synuclein inclusions in dopaminergic neurons in the substantia nigra. These results highlight an emergent potential toxin in anionic nanoplastics that might be explored further to better understand a possible role in PD risk and progression.

## Results

### Anionic nanoplastic contaminants catalyze $\alpha$ -synuclein aggregation

Sources and types of nanoplastics utilized in this study, along with empirically-derived measurements of particle diameters, are indicated in Table S1. To determine the effect of polystyrene nanoparticles on the aggregation of wild-type human  $\alpha$ -synuclein, we mixed a high concentration of  $\alpha$ -synuclein monomeric protein (i.e.,  $\sim 1$  mg per mL), free of high-molecular-weight aggregates (Fig. S1A,B), with 1 nM of  $\sim 39.5 \pm 0.7$  nm average diameter nanoplastics. Thus, the stoichiometry was  $\sim 1$  nanoplastic particle for every 70,000 monomer  $\alpha$ -synuclein particles (i.e.,  $\sim 74.8$   $\mu$ g per mL nanoplastic, or 0.007% w/v plastic in solution). This concentration of monomeric  $\alpha$ -synuclein (1 mg per mL, endotoxin-free) did not spontaneously aggregate on its own before  $\sim 10$  days of shaking at  $37^\circ\text{C}$  in phosphate-buffered saline (PBS) at pH 7.4, consistent with past reports (24, 25). Cellular concentrations of  $\alpha$ -synuclein protein in neurons are reported to be near 50  $\mu\text{M}$  (26). Continuous shaking of  $\alpha$ -synuclein with the nanoplastic contaminants produces hazy white foamy interfaces within a few days, and an overall turbid appearance by six days (Fig. 1A). Inspections of products in the solutions via negative-stain transmission electron microscopy (TEM) reveal the presence of multiple  $\alpha$ -synuclein fibrils emanating from single plastic particles in as early as 3 days (Fig. 1B). After 24 days of shaking, the overall composition of  $\alpha$ -synuclein fibrils under TEM are similar between nanoplastic-contaminated and nanoplastic-free reactions. To confirm that environmentally-derived polystyrene nanoplastic, which differs in surface coarseness from smoother engineered polystyrene nanoplastics (7), has a similar effect, we produced nanoplastics from single-use red Solo®-brand polystyrene plastic cups following National Institute of Standards and Technology (NIST) guidelines (27, 28). These particles, with a size distribution of  $115.6 \pm 34.3$  nm diameter, have a similar nucleating effect on  $\alpha$ -synuclein fibrils (Fig. S2). In contrast to the effects of anionic nanoplastics, charged graphene nanoparticles used in similar assays have the opposite effect in inhibiting aggregation (29), suggesting some level of specificity in how nanoparticles of different compositions interact with  $\alpha$ -synuclein.

To further explore the interaction between  $\alpha$ -synuclein and nanoplastics, we created binding assays using dynamic light scattering (DLS) to measure interactions between particles. The titration of  $\alpha$ -synuclein protein with a set amount of nanoplastic shows that one nanoplastic particle can form a stable complex with more than 100  $\alpha$ -synuclein monomers within minutes at room temperature (Fig. 1C,D). Evaluation of different concentrations of nanoplastics with

respect to a fixed concentration of  $\alpha$ -synuclein in real-time quaking induced conversion (RT-QuIC) assays show that low to sub-nanomolar concentrations of nanoplastic can nucleate the formation of  $\alpha$ -synuclein fibrils (Fig. 1E).

Previous studies using polyethylenimine-coated carboxyl-modified polystyrene nanoparticles showed a primary effect on the nucleation of  $\alpha$ -synuclein fibrils, with less of an effect on the seeded growth of fibrils (21). Binding assays show that nanoplastics also interact with pre-formed short  $\alpha$ -synuclein fibril seeds (Fig. S1A,B) within minutes of incubation at room temperature, at least  $\sim 10$  fibril particles per nanoplastic particle (Fig. 1F,G). In fibril seeded-nucleation reactions in aggregation assays, the anionic nanoplastic particles accelerate new fibril growth at low to subnanomolar concentrations (Fig. 1H). The interaction is charge dependent, as the addition of 400 nM sodium chloride to the solution prior to incubation of nanoplastic with  $\alpha$ -synuclein blocks interactions (Fig. S1C). These findings suggest that anionic nanoplastic particles interact with both monomeric and fibrilized forms of  $\alpha$ -synuclein in a potentially electrostatic-dependent manner.

### **Anionic nanoplastic bind the $\alpha$ -synuclein amphipathic and NAC domains to accelerate $\alpha$ -synuclein aggregation**

Nanoplastic particles are well known to passively and non-specifically (weakly) adsorb proteins (30, 31). In contrast to a non-specific interaction, molecular dynamic (MD) simulations suggest a stable  $\alpha$ -synuclein and anionic nanoplastic complex characterized by strong electrostatic attraction and compaction of the amphipathic domain and the adjoining non-amyloid component (NAC) domain (Fig. 2A). A similar complex did not form when the anionic nanoplastic was substituted for neutral and cationic nanoplastics (Fig. S3A-E). Likewise, calculated  $\Delta G_{\text{binding}}$  distributions indicate stronger associations with anionic than with neutral or cationic nanoplastics (Fig. 2B and Fig. S3F,G). Being the amphipathic and NAC hydrophobic domains of  $\alpha$ -synuclein are rich in positively charged lysine residues, we investigated further whether  $\alpha$ -synuclein aggregation results from electrostatic complementarity. Indeed, MD simulations reveal key hydrogen bonds and ionic intermolecular interactions drive anionic nanoplastics to specifically bind to residues in the amphipathic and NAC domains (Fig. 2C). The stacked bars in Fig. 2C indicates the sum of all interactions normalized to the length of the trajectory. For example, Lys80 has an average of 0.58 nanoplastic interactions, indicating it interacts with the nanoplastic 58% of the time. Thus both the amphipathic and NAC hydrophobic domains of  $\alpha$ -synuclein form strong interactions with anionic nanoplastic in the model.



Upon closer examination of the predicted complex, the anionic nanoplastic displaces water and intercalates between the amphipathic and NAC domains of  $\alpha$ -synuclein, potentially a key step in the eventual formation of  $\beta$ -sheets found in fibrils. Not only are the carboxylate groups able to form favorable polar and ionic interactions, the backbone of the polystyrene nanoplastic allows for good hydrophobic contact across the protein's surface between the carboxylate and ammonium pairs. Highlighted protein-ligand interactions (Fig. 2D and Fig. S4A,B) are predicted to be essential for the anionic nanoplastic binding to  $\alpha$ -synuclein, providing a potential nucleation site for  $\alpha$ -synuclein  $\beta$ -sheet stacking. Binding is reminiscent of some models for the  $\alpha$ -synuclein amphipathic domain interacting with different phospholipid compositions that also facilitate the eventual formation of  $\beta$ -sheets between NAC domains (32, 33), depending in-part on electrostatic interactions. These results are indicative of specific binding of anionic nanoplastic with  $\alpha$ -synuclein.

Interactions between nanoplastic and  $\alpha$ -synuclein protein fibrils were not evaluated in the same model since the structure of the amphipathic domain in  $\alpha$ -synuclein fibrils has not been defined according to the latest atomic models, though a similar interaction between  $\alpha$ -synuclein and the accessible (e.g., flexible) amphipathic domain in  $\alpha$ -synuclein fibrils are expected.

To investigate further whether the amphipathic domain of  $\alpha$ -synuclein is responsible for the interaction with anionic nanoplastic and the promotion of  $\alpha$ -synuclein aggregation, we created two truncated  $\alpha$ -synuclein proteins, one with half of the amphipathic domain removed and the other with the entire domain deleted (Fig. 3A). These proteins were purified to a high extent and confirmed to be monomeric (Fig. S5A-C). Our results show that without the amphipathic domain, the truncated proteins fail to interact with the anionic nanoplastic (Fig. 3B). These results support the molecular model, indicating anionic polystyrene's electrostatic complementarity paired with good hydrophobic contact is driving specificity for  $\alpha$ -synuclein and, therefore, nucleation. In addition, cationic polystyrene nanoplastic did not bind to the full-length  $\alpha$ -synuclein or the truncated proteins lacking the amphipathic domain. To investigate whether nanoplastic could promote  $\alpha$ -synuclein nucleation in the absence of the amphipathic domain, we conducted more aggregation assays. Although the truncated variants aggregate faster than the full-length  $\alpha$ -synuclein protein, the addition of anionic nanoplastic particles did not significantly stimulate their aggregation (Fig. 3C), indicating the necessity of the amphipathic domain both for binding and for interaction in aggregation.

These results suggest a possible strong interaction between anionic nanoplastic and the amphipathic domain of  $\alpha$ -synuclein. To test this prediction, we utilized surface plasmon resonance (SPR, Fig. S6A-C) to measure interaction strength between the nanoplastics and  $\alpha$ -synuclein. Full-length human  $\alpha$ -synuclein monomer has an exceptionally high affinity of  $\sim 2$  nM  $K_d$  with anionic nanoplastic at physiological buffer and pH conditions (Fig. 3D). However, binding estimates could not be obtained accurately for  $\alpha$ -synuclein affinity to nanoplastics when the protein lacks part or all of the amphipathic domain, or for full-length human  $\alpha$ -synuclein with cationic nanoplastic, ostensibly due to relatively weak interactions (Fig. S6). Affinity between nanoplastics and full length  $\alpha$ -synuclein fibrils further increases to  $\sim 0.03$  nM  $K_d$ , characteristic of an exceptionally strong interaction with aggregated  $\alpha$ -synuclein (Fig. S6F). Overall, these findings argue against a passive and non-specific adsorbance interaction between  $\alpha$ -synuclein and nanoplastics. Tight binding of  $\alpha$ -synuclein to nanoplastics might drive domain rearrangements that favor the formation of protein fibrils that also have high affinity for nanoplastics.

### **Anionic nanoplastics contaminants accelerate fibril-seeded $\alpha$ -synuclein pathology in neurons**

The mechanisms of neuronal uptake of anionic nanoplastic contaminants has not been extensively studied in the past, but the uptake of small exogenous  $\alpha$ -synuclein fibrils into neurons has been reported as dynamin-1 dependent (34). Latex-type microspheres (e.g., retrobeads) are often used as retrograde tracers in the brain and other organs. Nanoplastics internalize into NeuN-positive mature neurons (day-in-vitro DIV 7 mouse primary hippocampal neurons) within a few hours (Fig. 4A). Neurons composed more than 70% of the cells in the cultures (Fig. S7A,B). Within 12 hours after uptake, most of the particles in tau-positive cells (e.g., neurons) localize to LAMP1-positive vesicles (e.g., lysosomes, Fig. 4B, Fig S8A-C). To understand the endocytotic uptake mechanism related to anionic nanoplastic internalization in these neurons, and potential intersection with  $\alpha$ -synuclein in the endolysosomal compartment, we incubated neurons with nanoplastics of different sizes (Fig. 4C,D and Table S1) and with inhibitors of different types of endocytosis (Fig. 4E,F and Fig S8D,E). The clathrin-dependent endocytosis blockers Dynasore and PitStop2 (35, 36) effectively impair the internalization of nanoplastics into neurons (Fig 4E,F). In contrast, control dextran particle internalization is unaffected by these drugs, since dextran internalization occurs in neurons primarily via fluid-

phase endocytosis (37). The pH-sensitive dye labeling (i.e., pHrodo-Red) of the nanoplastics helps exclude the possibility of recording co-localization signals from non-internalized particles in the confocal sections, and neither the endocytosis inhibitors nor the nanoplastics had effects on endolysosomal acidity that might otherwise obscure fluorescence intensities (Fig. S9A,B). These results suggest that neurons (at least mature hippocampal neurons in culture) can rapidly internalize charged nanoplastics of different sizes largely through a clathrin-mediated mechanism.

Some past reports suggest nanoparticles composed of silica may have adverse effects on lysosome function in neurons and the clearance of amyloid (38). As opposed to treatments with the lysosome damaging agent L-leucyl-L-leucine methyl ester (LLOME), nanoplastic exposure does not cause the accumulation of the lysosomal damage marker galectin3 (Gal3) on LAMP1 vesicles in neurons (Fig 5A,B). However, reduced LysoSensor fluorescence observed for both nanoplastic and LLOME treatments might be indicative of a mild lysosomal impairment (e.g., deacidification, Fig 5C,D). As the lysosome has been described as the principle degradative organelle in neurons that metabolizes both endogenous low-molecular weight  $\alpha$ -synuclein as well as  $\alpha$ -synuclein aggregates (39–42), we created a BODIPY-labeled dye-quenched  $\alpha$ -synuclein fibril tool (i.e. dye-quenched, or DQ- $\alpha$ -synuclein) to measure the degradation of  $\alpha$ -synuclein at the neuronal lysosome. Fluorescence of the DQ- $\alpha$ -synuclein fibrils only occurs with proteolytic digestion. Consistent with the effects of LLOME exposures, nanoplastics attenuate the degradation of  $\alpha$ -synuclein fibrils in neurons both shortly after uptake and localization (at 12 hours) to LAMP1 positive vesicles, and at extended time points after internalization (48 hours, Fig 5E,F). Despite the effects on lysosome and  $\alpha$ -synuclein degradation impairment, there are no reductions observed in the numbers of NeuN positive cells in culture with nanoplastic treatments (Fig S10A), loss of tau neuronal processes (Fig S10B), or increases in nuclear permeability (i.e., toxicity, Fig S10C,D). Therefore, nanoplastic exposure at these concentrations appears well-tolerated, despite the mild lysosomal impairment. Incubation of  $\alpha$ -synuclein fibrils with proteinase K *in vitro* results in their degradation over time, observed through the loss of higher molecular weight proteins resolved by SDS-PAGE and immunoblot (43). The addition of different concentrations of nanoplastics to digestion reactions *in vitro* does not prevent the degradation of  $\alpha$ -synuclein fibrils by proteinase K (Fig 5G), suggesting that nanoplastic binding itself does not provide protection from proteases. These data suggest that nanoplastic impairment of the lysosome may be the principal factor in slowing the degradation of  $\alpha$ -synuclein aggregates.

Since both  $\alpha$ -synuclein fibrils and anionic nanoplastic uptake depend on dynamin-dependent endocytosis, we investigated whether these particles converge at the endolysosome to increase  $\alpha$ -synuclein aggregation. We have previously titrated different concentrations of human  $\alpha$ -synuclein fibril particles on primary neurons derived from non-transgenic mice, concluding that the addition of fibrils in the range of 10 to 100 pM induces robust pS129- $\alpha$ -synuclein pathology in as little as one-week (44). Combining labeled (AlexFluor-647)  $\alpha$ -synuclein fibrils (66.7 pM fibril particles, or  $\sim$ 1  $\mu$ g per mL  $\alpha$ -synuclein) with labeled (FITC) anionic nanoplastic results in the co-localization of nanoplastic and fibrils to LAMP1-positive vesicles in neurons within 12 hours (Fig. 6A,B). In testing different concentrations of nanoplastics on neurons, a modest concentration (1 nM of nanoplastic particles, or  $\sim$ 10  $\mu$ g per mL nanoplastic) increases pS129- $\alpha$ -synuclein pathology compared to neurons treated with only  $\alpha$ -synuclein fibrils, whereas lower nanoplastic concentrations (e.g., 10 pM) does not affect fibril-seeded inclusions within this time frame (Fig. S10E-G). The introduction of 1 nM unlabeled nanoplastic particles before the introduction of  $\alpha$ -synuclein fibrils, at the same time as fibril addition, or three-days after fibril addition, increases the amount of pS129- $\alpha$ -synuclein pathology at DIV 14 (Figure 6C-K). Potentially consistent with these observations, nanoplastic addition does not noticeably change the uptake of pHrodo-labeled  $\alpha$ -synuclein fibrils (Fig S11A,B). No immunohistochemical signals for pS129- $\alpha$ -synuclein could be resolved with nanoplastic only conditions, or vehicle controls. Biochemical evaluation of lysates from these treatments demonstrate that nanoplastics increase the deposition of  $\alpha$ -synuclein into insoluble protein fractions and the proportion of pS129- $\alpha$ -synuclein to total  $\alpha$ -synuclein protein (Fig 7A-C). High-resolution imaging shows that nanoplastic-induced pS129- $\alpha$ -synuclein pathology significantly increases the proportion of pathology that localizes to lysosomes (Fig 7D,E). However, the amount of pS129- $\alpha$ -synuclein pathology now at the lysosome with nanoplastic still represents the minority of overall recorded aggregates, suggesting typical intra-cellular spread of fibrils out of the endolysosomal compartment as expected in this model. Overall, these results indicate that anionic nanoplastic contaminants have potent (i.e., nanomolar) capacity to promote pS129- $\alpha$ -synuclein pathology in cultured neurons.

### **Anionic nanoplastics accelerate seeded pathological $\alpha$ -synuclein spread through the mouse brain**

Small  $\alpha$ -synuclein fibrils travel in both anterograde and retrograde directions away from injection sites in the mouse brain (45). Latex microbeads (e.g., acrylic latex) are effective retrograde tracers in neurons and other types of cells (46). However, the distribution and trafficking

patterns for anionic polystyrene nanoplastic contaminants, once inside the brain, have not been well studied. To explore the distribution of these nanoplastics in the brain after a single intracranial injection into the dorsal striatum, light sheet microscopy and confocal analysis show that labeled (FITC) nanoplastic particles on their own do not spread well from the injection site (Fig. 8A-C and Fig. S12A-C). In contrast,  $\alpha$ -synuclein fibrils distribute readily, accumulating in neurons in the cortex, thalamus, amygdala, and in dopaminergic neurons in the substantia nigra pars compacta (SNpc). The concentration of fibrils injected (4.5  $\mu$ g, single site) is an amount known to induce the production of hundreds of pS129- $\alpha$ -synuclein inclusions in these brain regions several months after the injection (44, 47). The co-injection of nanoplastics (15  $\mu$ g) with  $\alpha$ -synuclein fibrils results in a broadening of nanoplastic distribution similar to  $\alpha$ -synuclein fibril particles on their own (Fig 8D-F), with the noticeable exception of anterograde targets from the injection site (e.g., globus pallidus externa, or GPe). A lower concentration of 1.5  $\mu$ g of nanoplastic injected with the fibrils did not yield detectable nanoplastic particles in neurons (Fig. S12A), so we prioritized the higher 15  $\mu$ g nanoplastic injection to test for effects on accumulations in neurons and  $\alpha$ -synuclein aggregation.

With a co-injection of nanoplastics with  $\alpha$ -synuclein fibrils, ~20% of dopaminergic neurons in the SNpc three days post injection are positive for both  $\alpha$ -synuclein fibrils and nanoplastics in their cell soma, with about 75% of  $\alpha$ -synuclein fibril signal co-localizing with nanoplastic (Fig. 8D,E). Based on the robust observed colocalization between nanoplastic particles and  $\alpha$ -synuclein fibrils in neurons in the model, and the propensity of nanoplastics to stimulate  $\alpha$ -synuclein aggregation, we investigated whether the neurons harboring the nanoplastics might be more susceptible to form more  $\alpha$ -synuclein pathology. Similar to previous reports (45), human  $\alpha$ -synuclein fibrils injected into non-transgenic outbred CD1 mice poorly seeded phosphorylated pS129- $\alpha$ -synuclein positive inclusions through the cortex, amygdala, and SNpc (Fig. 9A,B). However, coadministration of nanoplastic together with the fibrils results in the formation of mature cytoplasmic pS129- $\alpha$ -synuclein inclusions in dopaminergic neurons (Fig. 9C), and a large overall increase in pS129- $\alpha$ -synuclein pathology across the cortical mantle, amygdala, and SNpc (Fig. 9D-F). No pS129- $\alpha$ -synuclein inclusions occurred in vehicle-only injected animals, and no overt neurodegeneration was present that might otherwise confound the analysis of the neuronal pathology (Fig. S13). Although a rare occurrence, we noted that three out of ten adult male mice injected in the striatum with only unlabeled anionic nanoplastics (no  $\alpha$ -synuclein protein) demonstrated several dopaminergic neurons each in the SNpc filled with pS129- $\alpha$ -synuclein pathology (Fig. 9G). These results suggest that anionic nanoplastics might be capable

of *de novo* induction of pS129  $\alpha$ -synuclein inclusions in dopaminergic neurons several months after the plastics are internalized by neurons in the brain.

### **Preliminary measurements of plastic pollution in human brain samples**

According to Leslie et al. (8), it is a common occurrence for blood samples to harbor (e.g., >1  $\mu$ g per mL) polystyrene contamination, and as opposed to other types of plastic pollution, nanoplastic polystyrene particles are known to cross the mammalian blood brain barrier (48). Recently, we reported strong  $\alpha$ -synuclein seeding activities observed in  $\alpha$ -synuclein aggregation assays in lysates from frozen frontal cortex brain tissues from Lewy body dementia cases (24). In adopting the protocol of Leslie et al. (8) that describes the sensitive detection of styrene fingerprint ions from lyophilized whole blood samples, frontal cortex brain tissues from Lewy body dementia with strong  $\alpha$ -synuclein seeding activity also yield strong styrene ion traces according to a double-shot pyrolysis gas-chromatography/mass spectrometry method (Figure S14). The styrene traces are unlikely to be from blood, as larger blood vessels were removed from the cortical brain tissue after lyophilization and before brain tissue pulverization. Further, the brain samples did not contact any polystyrene plasticware during processing (to our knowledge). In all cases, robust styrene ion traces were detected in both control and Lewy-body affected frontal cortex brain tissue, similar to the styrene ion traces previously described from healthy blood samples. However, different from that study, in brain samples, ions from other types of plastic (i.e., polypropylene or polyethylene) were not detected from the brain tissue pyrolyzates. It is important to note, as pointed out by others (8), these results are not definitive for the identification of polystyrene nanoplastic, and additional orthogonal methods will need to be developed to confirm the presence and concentrations of potential polystyrene particles in complex tissues like blood and brain. However, these data provide some of the first measurements for these contaminants that might be present as nanoplastics in human brain tissue.

## Discussion

Herein, our conclusions center on four main observations. First, anionic polystyrene nanoplastics bind the amphipathic domain of human wild-type  $\alpha$ -synuclein with very high affinity. Second,  $\alpha$ -synuclein binding to nanoplastic particles promotes  $\alpha$ -synuclein aggregation. Molecular modeling suggests this may be due to re-arrangement of NAC domain positioning and the displacement of water for negatively-charged polymer subunits between the domains. Third, both nanoplastic particles as well as exogenous  $\alpha$ -synuclein fibrils enter neurons in a large part through a clathrin-dependent endocytosis process, whereby both particles converge at the lysosome. Once inside neurons, anionic nanoplastics cause a mild-lysosomal impairment that slows the degradation of aggregated  $\alpha$ -synuclein, and upregulates the production of fibril-seeded pS129- $\alpha$ -synuclein inclusions. Finally, the coadministration of anionic nanoplastic contaminants with exogenous human  $\alpha$ -synuclein fibrils dramatically upregulates the spread of pS129- $\alpha$ -synuclein inclusions across interconnected brain regions in non-transgenic mice, including the formation of pathology in dopaminergic neurons in the SNpc. A hypothetical model that graphically summarizes these observations is presented in Fig. 10.

A biological context for these results can be inferred from other recent studies. Microplastic pollution and mammalian exposures to very small plastic particles is likely to increase for the foreseeable future (49). This is due to continued environmental degradation of older microplastics, for example through UV irradiation that can charge the particles and mechanical shearing that reduces average particle diameters (50). Therefore, it is relevant to explore the potential impact these emerging particles might have on disease risk, either risk imposed by particles currently in the environment that are difficult to measure with current technologies, or those that likely exist in the foreseeable future. Polystyrene microplastics, derived primarily from pervasive single-use plastics, have been identified in low microgram per milliliter quantities in blood samples from young healthy control subjects and may have the propensity to disrupt and cross the mammalian blood brain barrier to traverse into deep parenchymal brain tissue (8, 11–13, 51). Among other diseases potentially affected by nanoplastic exposures, PD is considered one of the fastest growing neurological conditions in the world, and emerging toxicants from the environment might impact disease risk in complex ways, for example, in interacting with other genetic susceptibilities (19, 52). The intersection of nanoplastics at the lysosome with  $\alpha$ -synuclein in neurons implicates a growing body of evidence that suggests lysosomal dysfunction may be at the heart of pathogenic mechanisms for PD risk (53). While PD has existed long before the rise of nanoplastics in the environment, nanoplastics exposures may

nevertheless present a new cumulative risk, depending on lifetime exposure levels, that can be explored in future studies. Here, the robust interaction between  $\alpha$ -synuclein and nanoplastics contaminants, coupled with the preliminary detection of polystyrene pollution in the human brain, may provide a rationale for further exploration related to nanoplastic exposures and PD risk.

*In vitro*, polystyrene contaminants bear a striking capacity at very low concentrations to promote seeding of  $\alpha$ -synuclein fibrils from otherwise soluble  $\alpha$ -synuclein protein. Interactions were noted with the  $\alpha$ -synuclein amphipathic domain that remains exposed in both monomeric protein and highly structured fibrils. While the concentration of native  $\alpha$ -synuclein at the synapse in healthy neurons has been estimated, whether or not anionic nanoplastics accumulate in neurons in humans (in health or disease) has not yet been evaluated to our knowledge. A vexing issue in nanoplastic research is that sensitive methods that might characterize the sizes of smaller nanoparticles derived from complex matrices like brain tissues and biofluids do not yet exist, so exposures are difficult to understand. While pyrolysis mass spectrometry methods like those employed here for human brain tissue analysis are sensitive to low parts-per-million, they do not divulge the sizes and exact molecular compositions of the parental polymers. Based on what is known in mammalian models, it seems unlikely that larger microplastics would be able to traverse through endothelial barriers and cells composing the blood brain barrier. However, as  $\alpha$ -synuclein seeding activity and pathology has been detected in the periphery including the gastrointestinal system of PD patients, nanoplastic contaminants need not necessarily invade the central brain to potentially corrupt  $\alpha$ -synuclein folding to impact disease risk or progression (29). Future studies are required to clarify these points.

From several different types of pervasive plastic waste types known, polystyrene nanoplastic was selected here because of the described action at the blood-brain barrier and positive detection in human blood. Other types of pervasive plastic waste such as polyethylenes, polycarbonates, or polypropylene may also interact with  $\alpha$ -synuclein (in the brain or periphery) and should be evaluated in future studies. The appearance of sparse but mature phosphorylated  $\alpha$ -synuclein inclusions in dopaminergic neurons in the midbrain of a few mice injected with only nanoplastics is a concerning result. According to a prion-like hypothesis for PD, these inclusions might spread to interconnected neurons and propagate through the brain, if given enough time. In humans, the detection of such sparse pathology might be consistent with a pathological diagnosis of incidental Lewy body disease. Some have hypothesized that incidental Lewy body disease is a precursor to PD and other Lewy-body diseases (54). Further



evaluation of plastic exposures with mice bearing additional risk factors for PD that might impair the neuronal lysosome, like advanced age, a *GBA1* mutation, or a *LRRK2* mutation, may be informative.

The combined injection of human  $\alpha$ -synuclein fibrils with nanoplastic contaminants highlights a strongly synergistic effect on the formation of inclusions in vulnerable brain regions in the mice. Perhaps a neuron harboring negatively charged nanoplastic at the acidic lysosome in the cell body would be more likely to develop an  $\alpha$ -synuclein inclusion than a healthy lysosome that readily degrades protein aggregates before they can propagate. Together these initial results in models highlight a potential toxin challenge in charged nanoplastics for further exploration in PD-related mechanisms. Future studies utilizing physiologically relevant nanoplastic exposures, as they continue to be defined in the environment, in combination with long-duration progressive PD-related models, will better inform emergent environmental risks.

## Materials and Methods

### Nanoplastics and particle sizing

Table S1 lists the different types of plastic particles catalog numbers used in each experiment in this study. To generate dye-labeled particles, polystyrene nanoplastic particles (at a concentration of 5 mg per mL) carrying amine surface modifications were incubated with 100  $\mu$ g per mL of pHrodo iFL Red STP ester, amine reactive dye (ThermoFisher, Cat# P36010) in 0.1 M sodium bicarbonate buffer, pH 8.3. Free pHrodo iFL Red STP ester was neutralized using 100 mM Tris-HCl at pH 7.4 and removed using Zeba Spin Desalting Columns (ThermoFisher, Cat# 89889). pHrodo-conjugated 10 kDa dextran was from ThermoFisher (P10361). To generate nanoplastics with mechanical stress, a custom abrasion machine was utilized as previously described (27). First, a plastic cup with polystyrene indicated as the main component was cut into 2.5 cm<sup>2</sup> pieces for mechanical abrasion. The sample was attached to the machine sample holder, and a 2 kg weight provided a normal force pressure while abrasion took place using P80 aluminum-oxide sandpaper (VWR, Cat# 296102). The sample was pressed against the abradant and rotated using a motor at a constant speed around 800-1000 RPM. The sample was enclosed in a chamber that was under a hosed fume extractor allowing for abraded microplastics to be collected for further analysis. To further generate nanoplastic particles, 0.5 g of microplastic powder was sonicated using a Fisher Scientific Sonic Dismembrator model 500 and 13 mm diameter probe tip at 30% power, 10 second pulse, 10 second off, for a total of 2 hours. The sonicated microplastic and nanoplastic mixture was passed through a syringe filter with 0.22  $\mu$ m pore size and concentrated to 200  $\mu$ L using an Amicon Ultra Centrifugal Filter Unit with 10 kDa molecular weight cutoff membrane (Millipore, Cat #MPUFC901024).

Particle number and size distribution of nanoplastic contaminants were analyzed using a ZetaView PMX-110 light scattering video microscope (Particle Metrix, Meerbusch, Germany) as previously described (55), and a Titan DynaPro (Wyatt Technology) for dynamic light scattering (DLS) analysis, at ~25°C. For DLS, the size distribution was analyzed using the Dyna V6.3.4 software package. For all measurements, samples were diluted in PBS (phosphate-buffered saline, pH 7.4). For ZetaView, tracking measurements were recorded and analyzed for 3 video cycles at each of 11 positions. Two-second video recordings at a rate of 30 frames per second were taken for each cycle. Video captures were analyzed using ZetaView Software 8.04.02 SP3, with specific parameters set as follows: maximum area: 5000, minimum area: 10, maximum brightness: 25, minimum brightness: 15, tracking radius: 100, minimum trace length: 20, shutter: 100, sensitivity: 92. The molarities reported for the particles are calculated from the particle number of the different preparations.

### Purification of recombinant human wild-type $\alpha$ -synuclein, truncated variants, and fibrils

cDNA encoding human  $\alpha$ -synuclein was synthesized and subcloned into pET21 bacterial expression plasmid. BL21 (DE3-RIL) CodonPlus cells (Agilent, Cat# 230245-41) were cultured in broth (ThermoFisher, Cat# 10855001) to optical density at 600 nm wavelength ( $OD_{600}$ ) = 0.8 at 37 °C before supplementation with 0.5 mM isopropyl  $\beta$ -D-1-thiogalactopyranoside (IPTG) to induce  $\alpha$ -synuclein expression for an additional 16 hours at 18°C, followed by centrifugation.

Cell pellets were lysed in 10 mM Tris–HCl, pH 7.6, 0.75 M NaCl, 1 mM EDTA, and 1 mM phenylmethylsulfonyl fluoride (PMSF), and sonicated at 70% power (Fisherbrand, Model 500 Dismembrator) for 1 min. Lysate was incubated in boiling water for 15 min before centrifugation. The supernatant was collected and dialyzed into 10 mM Tris–HCl, pH 7.6, 50 mM NaCl, 1 mM EDTA, and 1 mM PMSF before being loaded to a HiPrep Q HP 16/10 Column, 1 × 20 mL (GE Healthcare, Cat# 29018182) with a low-salt buffer containing 10 mM Tris–HCl pH 7.6, 25 mM NaCl, and eluted with a linear gradient of high-salt buffer (10 mM Tris–HCl, pH 7.6, and 1 M NaCl). Eluted fractions containing single bands for  $\alpha$ -synuclein (analyzed through Coomassie staining after SDS-PAGE, Fig. S1) were combined, dialyzed with PBS, and concentrated to 15 mg per mL. As endotoxin has a strong effect on  $\alpha$ -synuclein fibrillization, endotoxin in the purified recombinant  $\alpha$ -synuclein was removed using depletion columns (GenScript, Cat# L00338). Iterative column passes were performed until the final endotoxin level was < 0.1 unit per mg of protein, as determined by LAL chromogenic endotoxin quantification (GenScript, Cat# L00350C).

To generate pre-formed  $\alpha$ -synuclein fibril seeds, 5 mg per mL (~350  $\mu$ M) of purified human  $\alpha$ -synuclein in endotoxin-free PBS buffer was incubated in a tube mixer (Eppendorf, Thermomixer Compact 5350 Mixer) at 37°C with continuous agitation at 800 R.P.M. for the indicated time interval or 5-days. Pelleted and PBS-washed  $\alpha$ -synuclein fibrils were sonicated using a cup horn sonicator (Q-Sonica, Model Q700) with an active liquid cooling system that maintained the chamber temperature at 10°C. Some experiments required labeled  $\alpha$ -synuclein fibrils. To generate Alexa-647, pHrodo, or BODIPY-FL conjugated  $\alpha$ -synuclein fibrils,  $\alpha$ -synuclein fibrils were incubated with 100  $\mu$ g per mL of Alexa Fluor 647 NHS Ester (ThermoFisher, Cat# A20006) or pHrodo iFL Red STP Ester (ThermoFisher, Cat# P36010), or BODIPY-FL NHS ester (ThermoFisher Cat# D2184) in 0.1 M sodium bicarbonate buffer, pH 8.3, for 1 hour at room temperature. Free dyes were neutralized using 100 mM Tris-HCl at pH 7.4 and removed through differential centrifugation and extensive washing of the fibril pellets in PBS. Absorbance values corresponding to the free dyes were monitored until values returned to background levels, indicating the complete removal of free dyes. Dye-quenched (DQ)- $\alpha$ -synuclein refers to BODIPY-FL labeled  $\alpha$ -synuclein fibrils that have not been digested by proteases and have little to no associated fluorescence under physiological conditions. Dye-conjugated  $\alpha$ -synuclein fibrils were washed at least 5 times before sonication to generate working fibril seeds.

### **$\alpha$ -Synuclein sedimentation and real-time quaking-induced conversion (RT-QuIC) analysis**

Human  $\alpha$ -synuclein was mixed with plastic nanoparticles at indicated concentrations in a mixer (Eppendorf, Thermomixer Compact 5350 Mixer) at 37°C with continuous agitation at 800 R.P.M. Products were separated by sedimentation into heavy insoluble (pellet) and soluble (supernatant) fractions through centrifugation at 150,000  $xg$  (Beckman MAX-XP). Pellets and the supernatants were resuspended into a 2x Laemmli sample buffer (Bio-Rad, Cat# 1610737EDU) and analyzed by SDS-PAGE followed by Coomassie blue stain. RT-QuIC analysis was performed as previously described (24). Human  $\alpha$ -synuclein was mixed with plastic as indicated, or pre-formed  $\alpha$ -synuclein fibril seeds. Reaction mixtures were supplemented with 10  $\mu$ M thioflavin-T (ThT, Sigma, Cat# T3516-25g) as indicated to detect  $\beta$ -sheet structure in the forming  $\alpha$ -synuclein fibrils, with baseline and background fluorescence

subtracted. All reactions were performed in ultra-low binding 384-well plates (Corning, Cat# 4588) with clear bottoms and sealed with foil (BioRad, Cat# MSF1001). Fluorescence was monitored on a FLUOstar Omega (BMG) plate reader at 37 °C for the indicated time with 60 s of shaking at 700 R.P.M. followed by 60 sec of resting. ThT signal was recorded every 30 min at 448±10 nm excitation and 482±10 nm emission. Threshold values ( $C_T$ , hours) correspond to the time needed to achieve 10% of the maximum FL intensity (background subtracted).

### ***In vitro* protease digestion assays**

Pre-formed  $\alpha$ -synuclein fibril seeds (125 nM) were prepared in the absence or presence of nanoplastic particles at the indicated concentration and incubated at ~25°C for 30 min. Equal amounts of proteinase K (20 nM, Thermofisher Sci, Cat# 25530015) were added to each reaction that were incubated at 37°C for 10 min. Reactions were quenched through the addition of a 2x Laemmli buffer and boiling at 95°C for 10 min. Reactions were analyzed for remaining  $\alpha$ -synuclein reactivity >17 kDa as resolved by SDS-PAGE. Proteins were transferred to 0.22  $\mu$ m nitrocellulose membranes and immunoblotting was performed using anti- $\alpha$ -synuclein antibody (Abcam, Cat# ab138501).

### **Surface plasmon resonance analysis**

Binding kinetics of the nanoplastic particles were performed using the Biacore T200 SPR biosensor system (Cytiva, Cat# 28975001). Monomeric full-length  $\alpha$ -synuclein and N-truncated variants in solution (35  $\mu$ M), or sonicated fibrils (64 nM), were conjugated to CM5 sensor chips (Cytiva, Cat# BR100399) using amine coupling chemistry at a 1:1 ratio of NHS (11.5 mg per mL N-Hydroxysuccinimide) and EDC (75 mg per mL 1-Ethyl-3-(3-dimethylaminopropyl)carbodiimide hydrochloride)). Prior to immobilization, pre-concentration series were conducted with  $\alpha$ -synuclein proteins in 10 mM sodium acetate, pH 4.0 - 5.0, to select efficient conjugation conditions for each protein. Activation of the chip was 420 sec followed by immobilization steps for 30, 60, 120 secs until an increase in SPR intensity of 200-1000 response units (RUs) was observed. Deactivation of the surface was conducted by adding 1.0 M ethanolamine hydrochloride-NaOH at pH 8.5 at a 12 min contact time with the running buffer "HBS-EP+" (Cytiva, Cat #BR100669). For kinetic analysis, ligands were injected at flow rate of 50  $\mu$ L per min with contact times of 180 sec, dissociation times of 600 sec, and data collection rates of 10 Hz at ~25 °C. Regeneration at the end of the kinetic program was conducted at 50  $\mu$ L per min for 30 sec, with 10 sec of stabilization period using 10 mM glycine, pH 2.0, to remove bound particles and normalize the chip for the next cycle. Biacore Evaluation software was applied for kinetics analysis. Sensorgrams were reference-subtracted and analyzed using a heterogeneous ligand binding model to extract kinetic values from triplicate runs.

### **Computational approaches**

Using Spartan 20 (<https://www.wavefun.com/>), an equilibrium geometry calculation was performed on a 20-mer of neutral nanoplastic. The method was as follows: Density-function theory (DFT) = B3LYP 6-311+G\*\*, total charge = 0, unpaired electrons = 0, solvent = conductor-

like polarizable continuum model (CPCM), *dielectric* = 78.3 (water). The DFT optimized neutral nanoplastic structure was exported to “SDF” format and transferred to Maestro (Schrödinger, Inc.). The System Builder task was launched to generate a solvent boundary for simulation. The method was as follows: *solvent model* = simple-point charge (SPC), *box shape* = orthorhombic, *box size* = buffer, 20 Å x 20 Å x 20 Å, *exclude ion and salt placement within 20 Å of ligand*, *neutralize model by adding Na<sup>+</sup> or Cl<sup>-</sup> ions*, and *add 0.15 M NaCl*. The Molecular Dynamics (MD) task was launched, and the solvated system was simulated for 50 ns utilizing Desmond. The method was as follows: *simulation time* = 50 ns, *recording interval* = 50.0 ps, *ensemble class* = NPT, *temperature* = 310.15 K, *pressure* = 1.01325 bar. To produce the anionic nanoplastic, the MD converged/optimized neutral nanoplastic was functionalized at the *para*-positions of the phenyl rings with carboxylate groups. Adopting a previously reported model (7) of anionic nanoplastic, eight carboxylate groups were added across the nanoplastic 20-mer at every second phenyl group functionality. A solvated model of anionic nanoplastic was prepared and simulated using identical parameters for neutral nanoplastic. To produce cationic nanoplastic, the carboxylate groups of anionic nanoplastic were replaced with ammonium groups and also simulated using identical parameters for neutral nanoplastic. Desmond MD jobs were processed on the Duke Compute Cluster.

Human wild-type  $\alpha$ -synuclein monomer structure (PDB 1XQ8) was imported and prepared with the Protein Preparation Workflow task. Preprocessing was performed with the following parameters: *fill in missing side chains*; *assign bond orders*, using Combined Chemical Dictionary (CCD) database; *replace hydrogens*; *create zero-order bonds to metals*; *create disulfide bonds*; *fill in missing loops using Prime*; *sample water orientations*, use crystal symmetry, *minimize hydrogens of altered species*, use PROPKA with pH = 7.4; *restrained minimization was then performed*, converging heavy atoms to RMSD of 0.3 Å using OPLS4; *waters were removed 3.0 Å beyond het groups*. With the protein and nanoplastic ligands prepared, Induced Fit Docking (IFD) was launched to dock the nanoplastics to  $\alpha$ -synuclein. The receptor box was centered about residues Met1, Val37, Lys45, and Ala85 with a box size of 46 Å (maximum allowed size) to capture the N-terminal region and allow for unbiased docking. Prime refinement was performed to optimize residues within 12.0 Å of the ligand poses. Glide redocking was performed on structures within 30.0 kcal/mol of the best structure, but keeping only the top 20 structures overall, using SP precision. Once IFD was completed, solvated models of the nanoplastics with  $\alpha$ -synuclein were prepared and simulated using a 10 Å x 10 Å x 10 Å orthorhombic buffer box and a simulation time of 500 ns; all other parameters were identical to those previously described for preparation of the nanoplastics.

For each of the nanoplastic-protein complexes, all frames from the Desmond trajectories were loaded into Visual Molecular Dynamics (VMD) and the final 300 ns (6001 frames) were exported to GROningen format. GROMACS (GROningen Machine for Chemical Simulations) was then used to extract every 10<sup>th</sup> frame (netting 601 frames) to create a PDB ensemble of each complex (56). The resulting complexes were analyzed for  $\Delta G_{\text{binding}}$  via FireDock (57). FireDock scoring algorithms account for Van der Waals interactions, atomic contact energy, electrostatic, and additional binding free energy estimations between the target and ligand.

The advanced options for Desmond MD jobs were left as default and are as follows: *Integration – RESPA integrator time step: bonded = 2.0 fs, near = 2.00, far = 6.00; Ensemble – thermostat method: Nose-Hoover chain, relaxation time = 1.0 ps; barostat method: Martyna-Tobias Klein, relaxation time = 2.0 ps, coupling style – isotopic; Coulombic interaction – short range method = cutoff, cutoff radius = 9.0 Å.* The relaxation process for the NPT ensemble was left as default. Details of the relaxation process are available in the Desmond user manual: (1) minimize with solute restrained (2) minimize without restraints (3) simulate in the NVT ensemble using a Berendsen thermostat with a simulation time of 12 ps, temperature of 10°K, a fast temperature relaxation constant, velocity resampling every 1 ps, non-hydrogen solute atoms restrained (4) simulate in the NPT ensemble using a Berendsen thermostat and Berendsen barostat with a simulation time of 12 ps, temperature of 10 K and a pressure of 1 atm, a fast temperature relaxation constant, a slow pressure relaxation constant, velocity resampling every 1 ps, non-hydrogen solute atoms restrained (5) simulate in the NPT ensemble using a Berendsen thermostat and Berendsen barostat with a simulation time of 24 ps, temperature of 300 K and a pressure of 1 atm, a fast temperature relaxation constant, a slow pressure relaxation constant, velocity resampling every 1 ps, non-hydrogen solute atoms restrained (6) simulate in the NPT ensemble using a Berendsen thermostat and Berendsen barostat with a simulation time of 24 ps, temperature of 300°K and a pressure of 1 atm, a fast temperature relaxation constant, and a normal pressure relaxation constant.

## Imaging

For transmission electron microscopy, nanoplastic particles and  $\alpha$ -synuclein proteins were applied to glow-discharged 300 mesh, carbon-only, copper grids (Ladd, Cat# 10873-25), followed by negative staining with 2% uranyl acetate (Polysciences, Cat# 21447-25). Grids were imaged with a JEM-2100Plus Electron Microscope (JEOL, USA, Peabody, MA) operated at 120 kV with nominal magnification at 10,000x or 30,000x. Images were collected on an AMTNanoSprint16 digital camera (AMT Imaging, Woburn, MA) camera.

For confocal imaging, a Zeiss 880 inverted confocal microscope was used in Airyscan mode. The X,Y position was set with a Märzhäuser linearly encoded stage attached to a Zeiss Observer Z.1 inverted stand. Imaging was performed with the 63x 1.4 NA oil-immersion plan-Apochromat objective. All signals were collected with the Airyscan spatial detector with the Master gain set to 835 (488/green and 561/red) or 831 (far red), with emission was controlled by filters and beam splitters to achieve the following wavelength ranges: 488/green 495-550 nm, 561/red 570-615 nm, and 633/far red LP 660 nm. Images were acquired sequentially by line scanning at 1.21  $\mu$ s per pixel with a line averaging of 2 and a pixel size of 0.043  $\mu$ m and frame size of 1712 pixels in x, y with a zoom of 1.8. The pinhole used in confocal imaging is effectively different in Airyscan mode in which the Airyscan spatial detector collects 1.25 Airy units and Airyscan processing gives approximately 400 nm resolution in the Z dimension. Zen black software used for image processing shows 0.4  $\mu$ m section thickness for both the 488 and 561 channels and 0.5  $\mu$ m for the far red channel. For 3D images, Z-stacks from optimal thicknesses underwent maximum intensity projection and were normalized using consistent intensity thresholds.

For live-cell imaging and widefield microscopy, imaging was accomplished on a Keyence Bz-x700 microscope with a 20x Plan-Apochromat objective. Images were collected in auto-generated grids generated by the Manufacturer's controller software (Keyence, Inc.) spread across wells of multi-well plastic tissue culture dishes in a semi-automated manner. All widefield microscopy images were analyzed with ImageJ software by raters naive to experimental group identity.

For light sheet microscopy, mice were transcardially perfused with PBS followed by 4% PFA. Whole heads were then collected and post-fixed in 4% PFA overnight at 4°C. Decalcification was done by immersing the tissue in 10% EDTA for 24 h at 4°C. The iDISCO protocol was then carried out as described (58, 59). Briefly, whole heads were dehydrated in increasing methanol/H<sub>2</sub>O series (20%, 40%, 60%, 80%, 100%, 100%, 1 h each), delipidated with methanol/dichloromethane (33%/66% for 3 h) followed by pure dichloromethane (2 x 15 min), and optically cleared with ethyl cinnamate (ECI). Cleared samples were imaged on a LaVision UltraMicroscope Blaze light sheet microscope (Miltenyi Biotec) using a 4x objective (0.1 N.A.) equipped with an organic solvent compatible immersion-corrected dipping cap. The excitation wavelengths were 488 nm and 640 nm and emission filters used were 525/50 nm and 680/30 nm. Whole heads were imaged immersed in ECI in the horizontal orientation at a z-step size of 2 µm with InspectorPro7.5.3 software using both left and right-side illumination and single field of view. 3D renditions were then created with Arivis Vision 4 D 3.1 (Arivis AG).

### **Primary neuron cultures**

All procedures involving mice were approved by the Duke Institutional Animal Care and Use Committee. Hippocampi of 1-day postnatal CD1 mice pups (Charles River, strain 022) were collected and digested using 20 units per mL of papain (Worthington, Cat# LS003126) in Hanks' Balanced Salt Solution (HBSS, ThermoFisher, Cat# 14025126) for 30 min at 37 °C. The cell suspension was passed through a cell strainer with 40 µm mesh size (Fisher Scientific, Cat# 08-771-1) before plating (ThermoFisher, Cat# 142485) in wells coated with 0.1 mg per mL poly-D-lysine (ThermoFisher, Cat# A3890401) in media containing neurobasal (ThermoFisher, Cat# 21103049) supplemented with 5% FBS, 1xB27 supplement (ThermoFisher, Cat# 17504044), 0.5 mM L-glutamine (ThermoFisher, Cat# 35050061), and 100 unit per mL of penicillin-streptomycin (ThermoFisher, Cat# 10378016). 12 hours later, plating media was removed and replaced with maintenance media (neurobasal media supplemented with B27 and 0.5 mM L-glutamine). The cells were cultured 7 days (DIV 7) prior to usage in experiments.

### **Endocytosis and intra-neuronal localization assays**

For endocytosis assays, neurons were treated with 0.001% dimethylsulfoxide (DMSO, vehicle control), or 50 µM ethyl-isopropyl amiloride (EIPA), 50 µM dynasore, 0.2 µM wortmannin, or 15 µM Pitstop 2 (Abcam Cat#ab120687), or 2 mM methyl-β-cyclodextrin (MβCD) for 30 mins before incubation with pHrodo-conjugated polystyrene nanoparticles or dextran particles. The average uptake level per cell was calculated by dividing fluorescence intensity by the Hoechst positive particle (intact cell) count. For measurements related to endolysosome acidification, neurons were incubated with LysoSensor Green DND-189 (ThermoFisher, Cat# L7535) and

then 100 ng per mL Hoechst dye, followed by washing and subsequent imaging. Relative LysoSensor green signal was calculated by dividing the fluorescence intensity by the Hoechst particle count, and normalization to controls.

For analysis related to measurements of neuronal toxicity, some cultures were incubated with 2.5  $\mu$ M propidium iodide (Sigma) and 100 ng per mL Hoechst dye for 10 min before fixation with 4% paraformaldehyde (PFA, Sigma). Fixed cells were stained with rabbit-NeuN (1:2000, ThermoFisher, Cat# 14H6L24), anti-Lamp1 (1:2000, Santa Cruz, Cat#sc-19992), anti-tau (1:1000, ThermoFisher, Cat# MA5-12808), with donkey anti-rabbit Alexa 555 (1:2000, ThermoFisher, Cat# A-31572) and donkey anti-mouse Alexa 488 (1:2000, ThermoFisher, Cat# A-21202) secondary antibodies, as indicated. Number of NeuN-positive cells and tau-positive pixels as a function of area were quantified using ImageJ.

For subcellular localization of internalized nanoparticles, neurons were treated with FITC-conjugated polystyrene nanoparticles (Table S1) for the indicated time and cells were washed 3 times with PBS, fixed with 4% PFA, and immunostained for the indicated markers. The percentage of FITC pixels inside of LAMP1 positive endolysosomes in Airyscan images were quantified using ImageJ.

### **Fibril-seeded $\alpha$ -synuclein aggregation in primary neurons**

Neurons were treated with the indicated concentration of pre-formed sonicated  $\alpha$ -synuclein fibrils (Fig S1). At endpoints, cells were then washed with PBS, fixed with 4% PFA, and immunostained with anti-tau (1:1000, Invitrogen, MA5-12808), and anti-pS129- $\alpha$ -synuclein (1:2000, Abcam, ab51253) followed by staining with donkey anti-rabbit Alexa 555 (1:2000, ThermoFisher, Cat# A-31572) and donkey anti-mouse Alexa 488 (1:2000, ThermoFisher, Cat# A-21202), with DAPI (Sigma) dye. In obtained images, the area of pS129- $\alpha$ -synuclein-positive pixels was divided by the area of tau positive pixels. To analyze the soluble and insoluble development of  $\alpha$ -synuclein in primary hippocampal neurons, cells were lysed in 25 mM Tris, pH 7.4, 100 mM NaCl, 1x protease inhibitors (Roche, Cat# 04693116001), and 1x phosphatase inhibitors (Roche, Cat# 4906845001), followed by centrifugation at 50 xkg. The supernatant was collected as the soluble fraction. The pellets were resuspended in a lysis buffer with 2x Laemmli buffer and analyzed by SDS-PAGE followed by immunoblotting using anti-pS129- $\alpha$ -synuclein (1:5000, Abcam, Cat# ab51253), anti- $\alpha$ -synuclein (1:5000, Abcam, Cat# ab1903), or anti-human- $\alpha$ -synuclein (1:5000, Abcam, Cat# ab80627) antibodies.

### **Mouse intracranial injections and tissue staining**

Intracranial injections of nanoparticles and/or  $\alpha$ -synuclein fibrils, or vehicle control were performed as previously described (44). Male wild-type outbred CD1 mice obtained from Charles River were randomized to groups spread across multiple cages. Mice were used for experiments at 3 months of age. While power calculations were not performed, since the measures and models reported here use a model not previously described, group sizes of N=8-12 were approximated based on a previous publication that evaluated pS129- $\alpha$ -synuclein pathology resultant from the injection of human pre-formed  $\alpha$ -synuclein fibrils into the dorsal



striatum in wild-type mice (45). Mice were anesthetized with vaporized isoflurane and dexdomitor on a stereotaxic frame (Kopf Instruments). Solutions for injection were drawn to a 32-gauge custom needle (Hamilton) fitted to a gas-tight syringe and controlled by a digital pump (Harvard Apparatus). 3  $\mu$ L of solution containing the indicated amount of plastic or  $\alpha$ -synuclein fibrils, or vehicle control, was injected into the right dorsal striatum relative to Bregma: 1.0 mm anterior, 1.85 mm lateral, and 3.0 mm ventral relative to the skull. Scalp incisions were closed by suture. 3-days, or two months post-injection (as indicated), mice were deeply anesthetized with isoflurane and transcardially perfused with PBS followed by freshly prepared 4% paraformaldehyde (PFA) buffered in PBS. Brains were removed, post-fixed for 24 hours in 4% PFA and PBS solution, floated into 30% sucrose PBS solution for two days, and then cut to 40  $\mu$ m on a freezing microtome (Leica SM2010 R Sliding Microtome).

Sections were incubated in an antigen retrieval buffer (10 mM sodium citrate, 0.05% Tween 20, pH 6.0) for 1 hour with gentle rocking at 37 °C before being rinsed and incubated with tris-buffered saline (TBS, ThermoFisher, Cat# J60764.K2) with 5% donkey serum and 0.3% Triton X-100 for 1 hour. To detect  $\alpha$ -synuclein pathology, sections were incubated with primary antibodies including anti-tyrosine hydroxylase (1:2000, MilliporeSigma, Cat# AB1542 ), anti- $\alpha$ -synuclein (phospho S129) antibody (1:4000, Cat# EP1536Y, Abcam), or anti-NeuN antibody (1:2000, ThermoFisher, Cat# 14H6L24) in TBS buffer supplemented with 5% donkey serum and 0.1% Triton X-100 for 24 hours before incubations with secondary antibodies including donkey anti-sheep Alexa 555 (1;2000, ThermoFisher, Cat# A-21436), donkey anti-rabbit Alexa 647(1;2000, ThermoFisher, Cat# A32795), or donkey anti-rabbit Alexa 555 (1;2000, ThermoFisher, Cat# A-31572) for 24 hours. Sections were mounted on superfrost slides with ProLong Gold Antifade Mountant (ThermoFisher, P36930). The number of pS129- $\alpha$ -synuclein positive cells and percent of area occupied by pS129- $\alpha$ -synuclein were calculated using ImageJ.

### **Statistical analyses**

Analyses were performed by investigators blinded to sample identity until final data curation using coded identifiers for sample lysates, slides, and mice. GraphPad Prism 9 or IBM SPSS Statistics were used in all statistical analyses. Data distributions were assessed by Shapiro–Wilk tests. Data with normal distribution were assessed by one-way ANOVA (with Tukey's group mean comparison post hoc test) or a two-tailed t-test for group comparisons. Data with non-normal distributions were assessed with Mann–Whitney tests. P values < 0.05 were considered significant. Datasets were plotted in GraphPad Prism or in R-studio.

## References

1. M. Carbery, W. O'Connor, T. Palanisami, Trophic transfer of microplastics and mixed contaminants in the marine food web and implications for human health. *Environ. Int.* **115**, 400–409 (2018).
2. M. Enfrin, L. F. Dumée, J. Lee, Nano/microplastics in water and wastewater treatment processes - Origin, impact and potential solutions. *Water Res.* **161**, 621–638 (2019).
3. A. A. Koelmans, N. H. Mohamed Nor, E. Hermesen, M. Kooi, S. M. Mintenig, J. De France, Microplastics in freshwaters and drinking water: Critical review and assessment of data quality. *Water Res.* **155**, 410–422 (2019).
4. R. E. J. Schnurr, V. Alboiu, M. Chaudhary, R. A. Corbett, M. E. Quanz, K. Sankar, H. S. Srain, V. Thavarajah, D. Xanthos, T. R. Walker, Reducing marine pollution from single-use plastics (SUPs): A review. *Mar. Pollut. Bull.* **137**, 157–171 (2018).
5. A. E. Schwarz, T. N. Ligthart, E. Boukris, T. van Harmelen, Sources, transport, and accumulation of different types of plastic litter in aquatic environments: A review study. *Mar. Pollut. Bull.* **143**, 92–100 (2019).
6. K. N. Fotopoulou, H. K. Karapanagioti, Surface properties of beached plastic pellets. *Mar. Environ. Res.* **81**, 70–77 (2012).
7. W. Wei, Y. Li, M. Lee, N. Andrikopoulos, S. Lin, C. Chen, D. T. Leong, F. Ding, Y. Song, P. C. Ke, Anionic nanoplastic exposure induces endothelial leakiness. *Nat. Commun.* **13**, 4757 (2022).
8. H. A. Leslie, M. J. M. van Velzen, S. H. Brandsma, A. D. Vethaak, J. J. Garcia-Vallejo, M. H. Lamoree, Discovery and quantification of plastic particle pollution in human blood. *Environ. Int.* **163**, 107199 (2022).
9. L. Hoelting, B. Scheinhardt, O. Bondarenko, S. Schildknecht, M. Kapitza, V. Tanavde, B. Tan, Q. Y. Lee, S. Mecking, M. Leist, S. Kadereit, A 3-dimensional human embryonic stem cell (hESC)-derived model to detect developmental neurotoxicity of nanoparticles. *Arch. Toxicol.* **87**, 721–733 (2013).
10. S. A. Kulkarni, S.-S. Feng, Effects of particle size and surface modification on cellular uptake and biodistribution of polymeric nanoparticles for drug delivery. *Pharm. Res.* **30**, 2512–2522 (2013).
11. S. Kashiwada, Distribution of nanoparticles in the see-through medaka (*Oryzias latipes*). *Environ. Health Perspect.* **114**, 1697–1702 (2006).
12. X. Liu, Y. Zhao, J. Dou, Q. Hou, J. Cheng, X. Jiang, Bioeffects of Inhaled Nanoplastics on Neurons and Alteration of Animal Behaviors through Deposition in the Brain. *Nano Lett.* **22**, 1091–1099 (2022).
13. C.-S. Yang, C.-H. Chang, P.-J. Tsai, W.-Y. Chen, F.-G. Tseng, L.-W. Lo, Nanoparticle-based in vivo investigation on blood-brain barrier permeability following ischemia and reperfusion. *Anal. Chem.* **76**, 4465–4471 (2004).

14. L. C. Katz, A. Burkhalter, W. J. Dreyer, Fluorescent latex microspheres as a retrograde neuronal marker for in vivo and in vitro studies of visual cortex. *Nature*. **310**, 498–500 (1984).
15. H. Qian, X. Kang, J. Hu, D. Zhang, Z. Liang, F. Meng, X. Zhang, Y. Xue, R. Maimon, S. F. Dowdy, N. K. Devaraj, Z. Zhou, W. C. Mobley, D. W. Cleveland, X.-D. Fu, Reversing a model of Parkinson's disease with in situ converted nigral neurons. *Nature*. **582**, 550–556 (2020).
16. K. Murali, K. Kenesei, Y. Li, K. Demeter, Z. Környei, E. Madarász, Uptake and bio-reactivity of polystyrene nanoparticles is affected by surface modifications, ageing and LPS adsorption: in vitro studies on neural tissue cells. *Nanoscale*. **7**, 4199–4210 (2015).
17. A. Lesniak, D. Kilinc, A. Blasiak, G. Galea, J. C. Simpson, G. U. Lee, Rapid Growth Cone Uptake and Dynein-Mediated Axonal Retrograde Transport of Negatively Charged Nanoparticles in Neurons Is Dependent on Size and Cell Type. *Small*. **15**, e1803758 (2019).
18. GBD 2015 Neurological Disorders Collaborator Group, Global, regional, and national burden of neurological disorders during 1990-2015: a systematic analysis for the Global Burden of Disease Study 2015. *Lancet Neurol*. **16**, 877–897 (2017).
19. E. R. Dorsey, T. Sherer, M. S. Okun, B. R. Bloem, The Emerging Evidence of the Parkinson Pandemic. *J. Parkinsons. Dis.* **8**, S3–S8 (2018).
20. D. Erskine, D. Koss, V. I. Korolchuk, T. F. Outeiro, J. Attems, I. McKeith, Lipids, lysosomes and mitochondria: insights into Lewy body formation from rare monogenic disorders. *Acta Neuropathol*. **141**, 511–526 (2021).
21. H. Mohammad-Beigi, M. Zanganeh, C. Scavenius, H. Eskandari, A. Farzadfard, S. A. Shojaosadati, J. J. Enghild, D. E. Otzen, A. K. Buell, D. S. Sutherland, A Protein Corona Modulates Interactions of  $\alpha$ -Synuclein with Nanoparticles and Alters the Rates of the Microscopic Steps of Amyloid Formation. *ACS Nano*. **16**, 1102–1118 (2022).
22. D. Kim, J. M. Yoo, H. Hwang, J. Lee, S. H. Lee, S. P. Yun, M. J. Park, M. Lee, S. Choi, S. H. Kwon, S. Lee, S.-H. Kwon, S. Kim, Y. J. Park, M. Kinoshita, Y.-H. Lee, S. Shin, S. R. Paik, S. J. Lee, S. Lee, B. H. Hong, H. S. Ko, Graphene quantum dots prevent  $\alpha$ -synucleinopathy in Parkinson's disease. *Nat. Nanotechnol*. **13**, 812–818 (2018).
23. X. Yuan, Y. Yang, D. Xia, L. Meng, M. He, C. Liu, Z. Zhang, Silica Nanoparticles Promote  $\alpha$ -Synuclein Aggregation and Parkinson's Disease Pathology. *Front. Neurosci*. **15**, 807988 (2021).
24. A. Sokratian, J. Ziaee, K. Kelly, A. Chang, N. Bryant, S. Wang, E. Xu, J. Y. Li, S.-H. Wang, J. Ervin, S. M. Swain, R. A. Liddle, A. B. West, Heterogeneity in  $\alpha$ -synuclein fibril activity correlates to disease phenotypes in Lewy body dementia. *Acta Neuropathol*. **141**, 547–564 (2021).
25. M. E. Bernis, J. T. Babila, S. Breid, K. A. Wüsten, U. Wüllner, G. Tamgüney, Prion-like propagation of human brain-derived alpha-synuclein in transgenic mice expressing human wild-type alpha-synuclein. *Acta Neuropathol Commun*. **3**, 75 (2015).

26. B. G. Wilhelm, S. Mandad, S. Truckenbrodt, K. Kröhnert, C. Schäfer, B. Rammner, S. J. Koo, G. A. Claßen, M. Krauss, V. Haucke, H. Urlaub, S. O. Rizzoli, Composition of isolated synaptic boutons reveals the amounts of vesicle trafficking proteins. *Science*. **344**, 1023–1028 (2014).
27. N. Bossa, J. M. Sipe, W. Berger, K. Scott, A. Kennedy, T. Thomas, C. O. Hendren, M. R. Wiesner, Quantifying Mechanical Abrasion of MWCNT Nanocomposites Used in 3D Printing: Influence of CNT Content on Abrasion Products and Rate of Microplastic Production. *Environ. Sci. Technol.* **55**, 10332–10342 (2021).
28. J. M. Sipe, N. Bossa, W. Berger, N. von Windheim, K. Gall, M. R. Wiesner, From bottle to microplastics: Can we estimate how our plastic products are breaking down? *Sci. Total Environ.* **814**, 152460 (2022).
29. S. Kim, S.-H. Kwon, T.-I. Kam, N. Panicker, S. S. Karuppagounder, S. Lee, J. H. Lee, W. R. Kim, M. Kook, C. A. Foss, C. Shen, H. Lee, S. Kulkarni, P. J. Pasricha, G. Lee, M. G. Pomper, V. L. Dawson, T. M. Dawson, H. S. Ko, Transneuronal Propagation of Pathologic  $\alpha$ -Synuclein from the Gut to the Brain Models Parkinson's Disease. *Neuron*. **103**, 627–641.e7 (2019).
30. S. Kihara, S. Ghosh, D. R. McDougall, A. E. Whitten, J. P. Mata, I. Köper, D. J. McGillivray, Structure of soft and hard protein corona around polystyrene nanoplastics-Particle size and protein types. *Biointerphases*. **15**, 051002 (2020).
31. S. Kihara, N. J. van der Heijden, C. K. Seal, J. P. Mata, A. E. Whitten, I. Köper, D. J. McGillivray, Soft and Hard Interactions between Polystyrene Nanoplastics and Human Serum Albumin Protein Corona. *Bioconjug. Chem.* **30**, 1067–1076 (2019).
32. E. Rhoades, T. F. Ramlall, W. W. Webb, D. Eliezer, Quantification of alpha-synuclein binding to lipid vesicles using fluorescence correlation spectroscopy. *Biophys. J.* **90**, 4692–4700 (2006).
33. T. Dou, L. Zhou, D. Kourouski, Unravelling the Structural Organization of Individual  $\alpha$ -Synuclein Oligomers Grown in the Presence of Phospholipids. *J. Phys. Chem. Lett.* **12**, 4407–4414 (2021).
34. M. Konno, T. Hasegawa, T. Baba, E. Miura, N. Sugeno, A. Kikuchi, F. C. Fiesel, T. Sasaki, M. Aoki, Y. Itoyama, A. Takeda, Suppression of dynamin GTPase decreases  $\alpha$ -synuclein uptake by neuronal and oligodendroglial cells: a potent therapeutic target for synucleinopathy. *Mol. Neurodegener.* **7**, 38 (2012).
35. E. Macia, M. Ehrlich, R. Massol, E. Boucrot, C. Brunner, T. Kirchhausen, Dynasore, a cell-permeable inhibitor of dynamin. *Dev. Cell.* **10**, 839–850 (2006).
36. L. von Kleist, W. Stahlschmidt, H. Bulut, K. Gromova, D. Puchkov, M. J. Robertson, K. A. MacGregor, N. Tomilin, A. Pechstein, N. Chau, M. Chircop, J. Sakoff, J. P. von Kries, W. Saenger, H.-G. Kräusslich, O. Shupliakov, P. J. Robinson, A. McCluskey, V. Haucke, Role of the clathrin terminal domain in regulating coated pit dynamics revealed by small molecule inhibition. *Cell*. **146**, 471–484 (2011).
37. Y. W. H. Koh, Y. Hung, N. Tuladhar, Z. Xiao, D. L. Brown, N. D. Condon, J. L. Stow, Live Fluorescence, Inverse Imaging of Cell Ruffling, and Macropinocytosis. *J. Vis. Exp.* (2021),

doi:10.3791/62870.

38. Y. Ye, L. Hui, K. L. Lakpa, Y. Xing, H. Wollenzien, X. Chen, J. X. Zhao, J. D. Geiger, Effects of silica nanoparticles on endolysosome function in primary cultured neurons. *Can. J. Physiol. Pharmacol.* **97**, 297–305 (2019).
39. A. N. Sacino, M. M. Brooks, P. Chakrabarty, K. Saha, H. Khoshbouei, T. E. Golde, B. I. Giasson, Proteolysis of  $\alpha$ -synuclein fibrils in the lysosomal pathway limits induction of inclusion pathology. *J. Neurochem.* **140**, 662–678 (2017).
40. S. K. Mak, A. L. McCormack, A. B. Manning-Bog, A. M. Cuervo, D. A. Di Monte, Lysosomal degradation of alpha-synuclein in vivo. *J. Biol. Chem.* **285**, 13621–13629 (2010).
41. A. M. Cuervo, L. Stefanis, R. Fredenburg, P. T. Lansbury, D. Sulzer, Impaired degradation of mutant alpha-synuclein by chaperone-mediated autophagy. *Science.* **305**, 1292–1295 (2004).
42. J. L. Webb, B. Ravikumar, J. Atkins, J. N. Skepper, D. C. Rubinsztein, Alpha-Synuclein is degraded by both autophagy and the proteasome. *J. Biol. Chem.* **278**, 25009–25013 (2003).
43. M. Neumann, P. J. Kahle, B. I. Giasson, L. Ozmen, E. Borroni, W. Spooren, V. Müller, S. Odoy, H. Fujiwara, M. Hasegawa, T. Iwatsubo, J. Q. Trojanowski, H. A. Kretzschmar, C. Haass, Misfolded proteinase K-resistant hyperphosphorylated alpha-synuclein in aged transgenic mice with locomotor deterioration and in human alpha-synucleinopathies. *J. Clin. Invest.* **110**, 1429–1439 (2002).
44. H. Abdelmotilib, T. Maltbie, V. Delic, Z. Liu, X. Hu, K. B. Fraser, M. S. Moehle, L. Stoyka, N. Anabtawi, V. Krendelchtchikova, L. A. Volpicelli-Daley, A. West,  $\alpha$ -Synuclein fibril-induced inclusion spread in rats and mice correlates with dopaminergic Neurodegeneration. *Neurobiol. Dis.* **105**, 84–98 (2017).
45. K. C. Luk, D. J. Covell, V. M. Kehm, B. Zhang, I. Y. Song, M. D. Byrne, R. M. Pitkin, S. C. Decker, J. Q. Trojanowski, V. M.-Y. Lee, Molecular and Biological Compatibility with Host Alpha-Synuclein Influences Fibril Pathogenicity. *Cell Rep.* **16**, 3373–3387 (2016).
46. L. C. Katz, D. M. Iarovici, Green fluorescent latex microspheres: a new retrograde tracer. *Neuroscience.* **34**, 511–520 (1990).
47. K. C. Luk, V. Kehm, J. Carroll, B. Zhang, P. O'Brien, J. Q. Trojanowski, V. M.-Y. Lee, Pathological  $\alpha$ -synuclein transmission initiates Parkinson-like neurodegeneration in nontransgenic mice. *Science.* **338**, 949–953 (2012).
48. S. Shan, Y. Zhang, H. Zhao, T. Zeng, X. Zhao, Polystyrene nanoplastics penetrate across the blood-brain barrier and induce activation of microglia in the brain of mice. *Chemosphere.* **298**, 134261 (2022).
49. D. M. Mitrano, P. Wick, B. Nowack, Placing nanoplastics in the context of global plastic pollution. *Nat. Nanotechnol.* **16**, 491–500 (2021).
50. W. Fu, J. Min, W. Jiang, Y. Li, W. Zhang, Separation, characterization and identification of microplastics and nanoplastics in the environment. *Sci. Total Environ.* **721**, 137561 (2020).

51. V. Kopatz, K. Wen, T. Kovács, A. S. Keimowitz, V. Pichler, J. Widder, A. D. Vethaak, O. Hollóczki, L. Kenner, Micro- and Nanoplastics Breach the Blood-Brain Barrier (BBB): Biomolecular Corona's Role Revealed. *Nanomaterials (Basel)*. **13** (2023), doi:10.3390/nano13081404.
52. B. R. De Miranda, S. M. Goldman, G. W. Miller, J. T. Greenamyre, E. R. Dorsey, Preventing Parkinson's Disease: An Environmental Agenda. *J. Parkinsons. Dis.* **12**, 45–68 (2022).
53. R. L. Wallings, S. W. Humble, M. E. Ward, R. Wade-Martins, Lysosomal Dysfunction at the Centre of Parkinson's Disease and Frontotemporal Dementia/Amyotrophic Lateral Sclerosis. *Trends Neurosci.* **42**, 899–912 (2019).
54. C. H. Adler, D. J. Connor, J. G. Hentz, M. N. Sabbagh, J. N. Caviness, H. A. Shill, B. Noble, T. G. Beach, Incidental Lewy body disease: clinical comparison to a control cohort. *Mov. Disord.* **25**, 642–646 (2010).
55. A. Mehdiani, A. Maier, A. Pinto, M. Barth, P. Akhyari, A. Lichtenberg, An innovative method for exosome quantification and size measurement. *J. Vis. Exp.*, 50974 (2015).
56. M. J. Abraham, T. Murtola, R. Schulz, S. Páll, J. C. Smith, B. Hess, E. Lindahl, GROMACS: High performance molecular simulations through multi-level parallelism from laptops to supercomputers. *SoftwareX*. **1-2**, 19–25 (2015).
57. N. Andrusier, R. Nussinov, H. J. Wolfson, FireDock: fast interaction refinement in molecular docking. *Proteins*. **69**, 139–159 (2007).
58. N. Renier, E. L. Adams, C. Kirst, Z. Wu, R. Azevedo, J. Kohl, A. E. Autry, L. Kadiri, K. Umadevi Venkataraju, Y. Zhou, V. X. Wang, C. Y. Tang, O. Olsen, C. Dulac, P. Osten, M. Tessier-Lavigne, Mapping of Brain Activity by Automated Volume Analysis of Immediate Early Genes. *Cell*. **165**, 1789–1802 (2016).
59. A. Ertürk, F. Bradke, High-resolution imaging of entire organs by 3-dimensional imaging of solvent cleared organs (3DISCO). *Exp. Neurol.* **242**, 57–64 (2013).

**Acknowledgements:** We thank Dr. Lisa Cameron and Duke Light Microscopy Core Facility for support of fluorescence microscopy image collection and analysis, Dr. Michael A. Peterson for assistance with and maintenance of Duke University Department of Chemistry Virtual Machine, and Duke University Research Computing for maintenance and providing use of the Duke Compute Cluster (DCC). For the purpose of open access, the author has applied a CC-BY public copyright license to the Author Accepted Manuscript (AAM) version arising from this submission.

**Funding information:** The study is funded by the joint efforts of The Michael J. Fox Foundation for Parkinson's Research (MJFF) and the Aligning Science Across Parkinson's (ASAP) initiative. MJFF administers the grant ASAP-020527 on behalf of ASAP and itself. This work was also supported by NIH/NINDS R01 NS064934, P50 NS108675 (A.B.W.); NIH/NIA 5K99AG075179-02 (Z. L.); National Science Foundation Graduate Research Fellowship NSF GRFP DGE-1644868 (J.S.); NIH/NEI Grant R01 EY031748 (to C.B.R.), and P30 EY005722 (to Duke Eye Center); Research to Prevent Blindness Grant (to the Duke Eye Center). NIH F31 EY033170, T32 HD040372 (B.H.); NIH Pharmacological Sciences Training Program T32 GM133352-02, and the Olle Engkvist Foundation (I.L.).

**Author Contributions:**

Conceptualization: ZL, AS, AD, EX, ABW

Methodology: ZL, AS, AD, EX, CS, IL, ABW

Investigation: ZL, AS, AD, EX, AF, SS, HL, YY, BB, JS, KB, NL, BH

Visualization: ZL, AS, AD, EX, CS, SS, BB, IL, NL, ABW

Supervision: IL, CBR, SM, ABW

Writing: original draft: ZL, AS, AD, SM, ABW

Writing-review & editing: ZL, AS, AD, ABW

**Competing Interests:** The authors declare they have no competing interests.

**Data and Materials Availability:** All data needed to evaluate the conclusions in the paper are present in the paper and/or the Supplementary Materials.

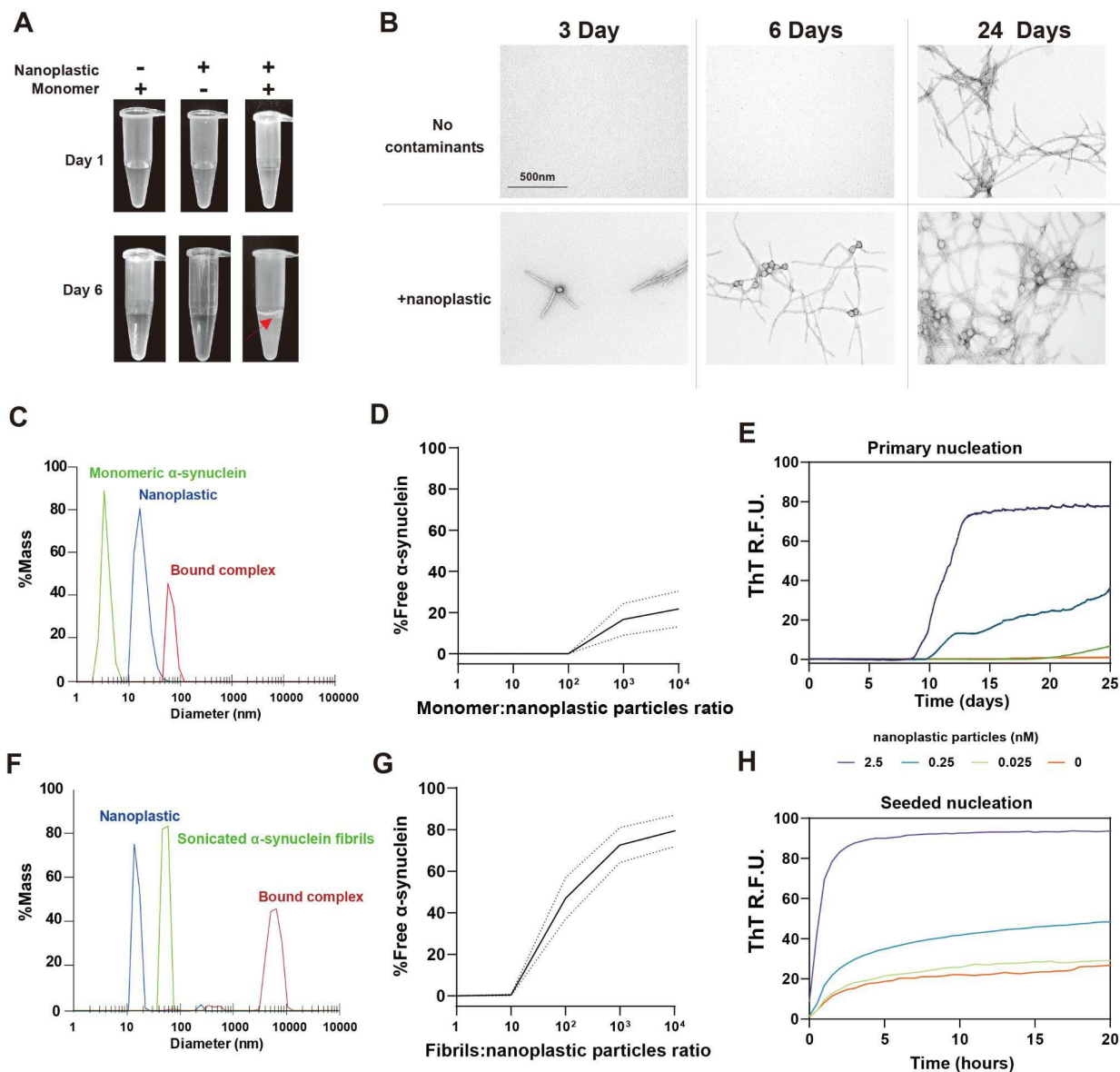


**Fig. 1 Nanoplastic contaminants complex with monomeric  $\alpha$ -synuclein at low stoichiometry to accelerate both spontaneous and seeded fibrillation *in vitro*.**

- A) Representative appearance of incubation products in centrifuge tubes with 70  $\mu$ M  $\alpha$ -synuclein monomer, with or without 1 nM nanoplastic particles mixed for 1 or 6 days with shaking at 37°C. Red arrow highlights turbidity and a white precipitating layer found with  $\alpha$ -synuclein mixed with nanoplastics after 6 days.
- B) Transmission electron microscopy (TEM) of the products of  $\alpha$ -synuclein incubations with or without nanoplastic contaminants incubated for 3, 6, and 24 days. Scale bar, 500 nm.



- C) Dynamic light scattering (DLS) profiles plotted to mass-distributions for monomeric  $\alpha$ -synuclein (green curve) and nanoplastic contaminants (blue curve). Products are from incubations (30 min, RT) at a molar ratio of 10:1 (protein to plastic, red curve).
- D) Calculated free monomeric  $\alpha$ -synuclein at different stoichiometries with nanoplastic after incubation (30 min, RT). Curve is mean with 95% CI as dashed lines.
- E) Spontaneous aggregation of  $\alpha$ -synuclein (70  $\mu$ M monomer) at 37°C with shaking in PBS assessed through thioflavin-T (ThT) fluorescence over time with increasing concentrations of nanoplastic contaminants. Each curve is the mean of six technical replicates repeated in three independent reactions.
- F) Representative DLS profiles that include small  $\alpha$ -synuclein fibrils (green curve, see Fig. S1 for characterization of fibrils). Incubations (30 min, RT) of  $\alpha$ -synuclein fibrils with nanoplastic are at a molar ratio of 10:1 (protein to plastic, red curve).
- G) Calculated free  $\alpha$ -synuclein fibrils at different stoichiometries with nanoplastics after incubation (30 min, RT). Curve is mean with 95% CI as dashed lines.
- H) ThT fluorescence over time, starting with 64 pM  $\alpha$ -synuclein fibril particles and 70  $\mu$ M monomer supplemented with the indicated concentration of nanoplastic contaminants. Each curve represents a mean of six replicates from three independent reactions.

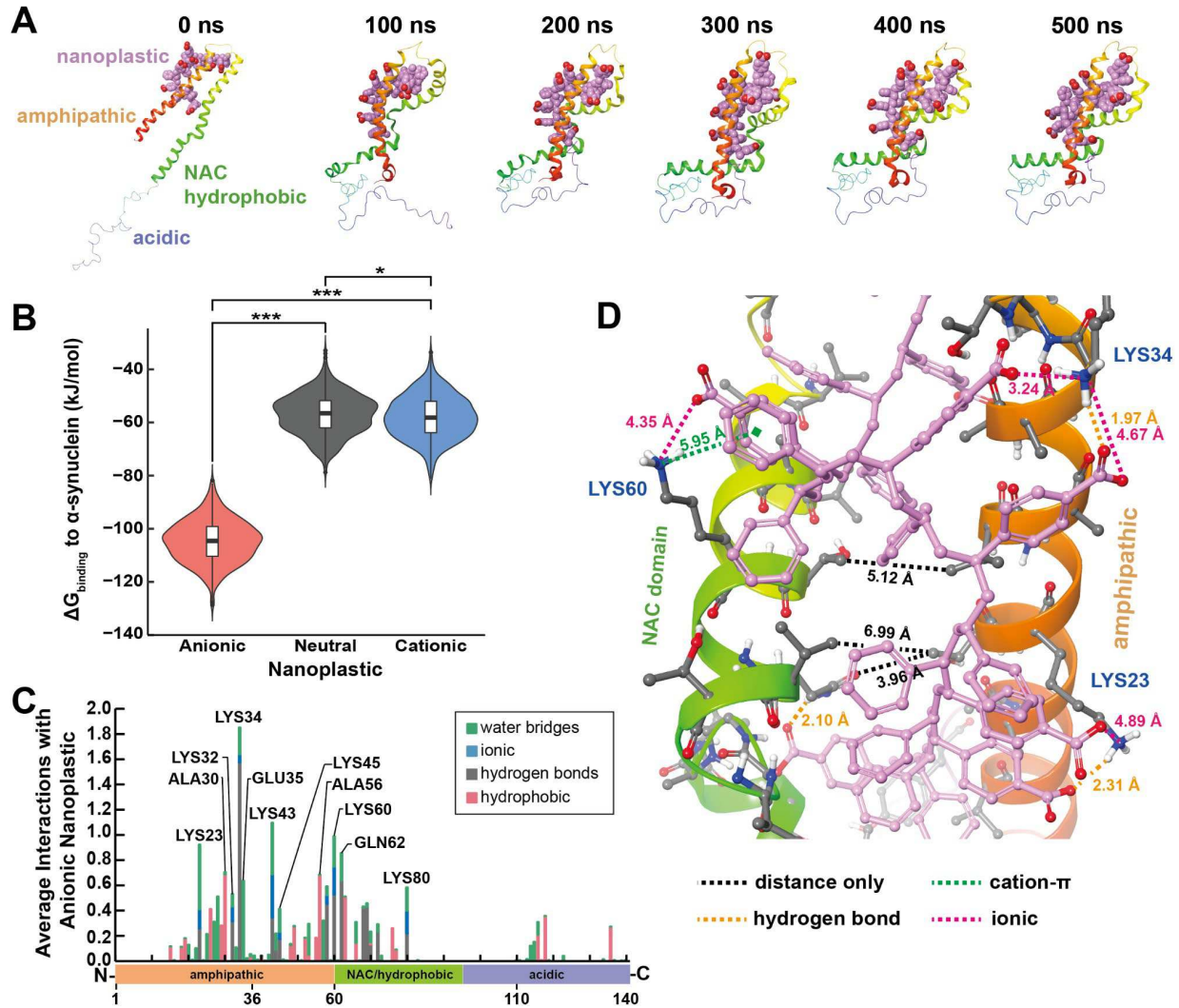


**Fig. 2. *In silico* modeling identifies a strong interaction between the amphipathic and NAC domains of  $\alpha$ -synuclein and anionic nanoplastic.**

- A) Snapshots at 100 ns intervals of anionic nanoplastic with monomeric  $\alpha$ -synuclein across molecular dynamics (MD) simulations. Key domains of  $\alpha$ -synuclein are indicated at 0 ns. Anionic nanoplastics are space-filled showing polar hydrogens only; pink = carbon, red = oxygen.  $\alpha$ -Synuclein monomers are depicted as ribbons colored by residue index.
- B) Violin plots overlaid with box-and-whisker plots representing the distribution of  $\Delta G_{\text{binding}}$  for each nanoplastic: $\alpha$ -synuclein complex from every tenth frame starting from 200 ns (N=601 each group), time at which each complex converged. See Fig S3 for more MD timeframes. \*p<0.05, \*\*\* p<0.001, one-way ANOVA with Tukey's post-hoc test.
- C) Histogram demonstrating the average number of interactions between  $\alpha$ -synuclein and anionic nanoplastics across converged MD simulation (200-500 ns), categorized by four intermolecular interaction types. Stacked bars indicate the sum of all interactions normalized to the length of the trajectory.

D) Representative image of anionic nanoplastic bridging the amphipathic and NAC domains of  $\alpha$ -synuclein. Distances between the amphipathic and NAC domains are depicted with black dashed lines. Intermolecular forces and their distances between anionic nanoplastic and  $\alpha$ -synuclein are indicated. Anionic nanoplastic, depicted as ball-and-stick, shows polar hydrogens only; pink = carbon, red = oxygen.  $\alpha$ -Synuclein (ribbons) are colored by residue index; white=hydrogen, grey=carbon, blue=nitrogen, red=oxygen.

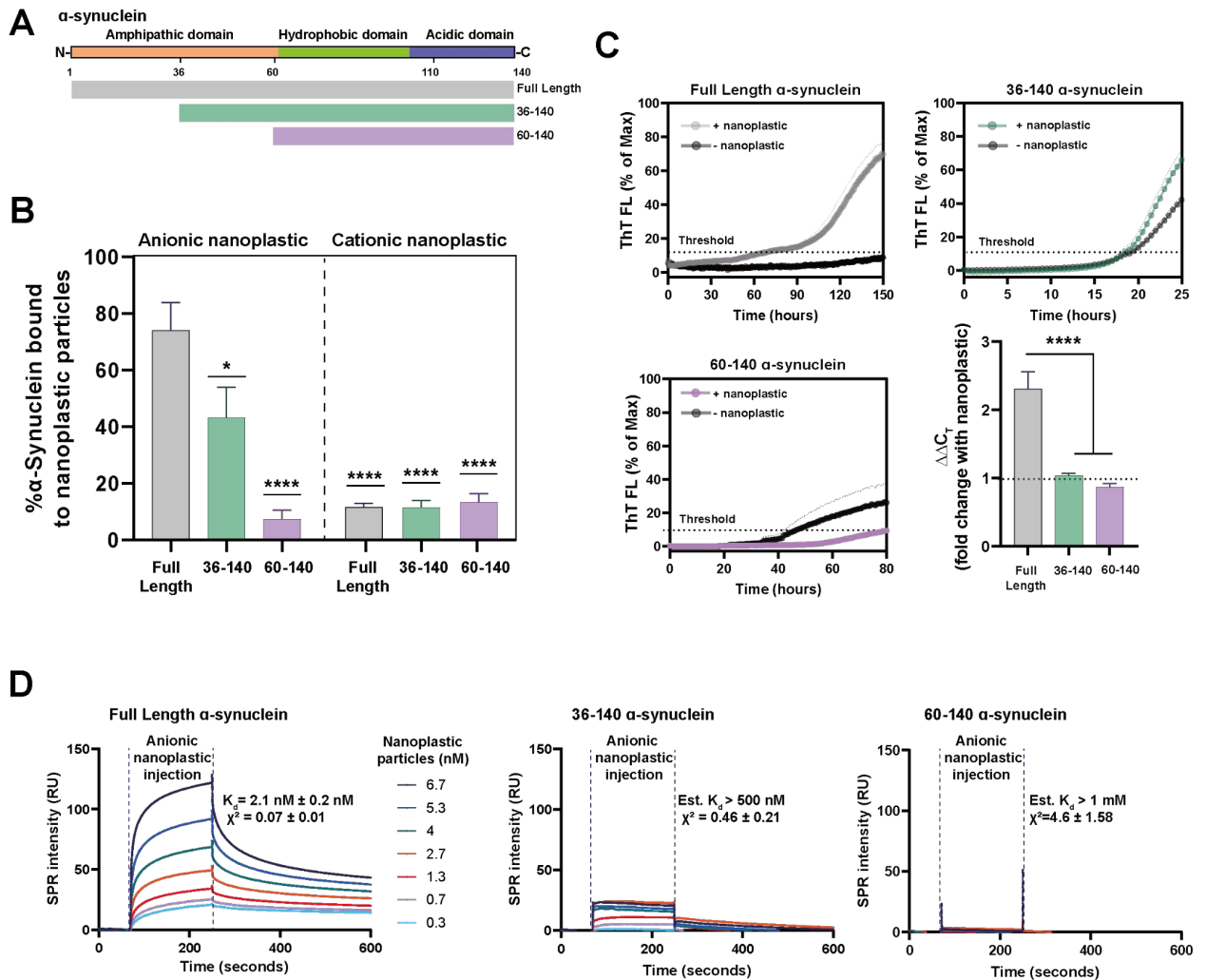


**Fig. 3. Anionic nanoplastic tightly binds to the  $\alpha$ -synuclein amphipathic domain to initiate fibrillation *in vitro*.**

- A) Domain structure of  $\alpha$ -synuclein. Aligned truncated variants in green (36-140) and purple (60-140) are aligned to full-length protein in gray (1-140).
- B) Column graphs showing the percentage of full-length, or truncated, monomeric  $\alpha$ -synuclein binding to nanoplastic particles (anionic or cationic). Dynamic light scattering (DLS) resolves complexes at a stoichiometry of 10:1 protein to nanoplastics. Bars represent mean values of 20 independent acquisitions (SEM shown). \*p<0.01, \*\*\*\*p<0.0001, one-way ANOVA with Dunnet's post-hoc test.
- C) Spontaneous full length or truncated  $\alpha$ -synuclein aggregation assessed through thioflavin-T (ThT) fluorescence over time, with or without 2.5 nM anionic nanoplastic particles as indicated. Curves represent mean values from quintuplicate independent reactions (SEM shown). Black dashed horizontal line indicates 10% ThT maximum fluorescence used to calculate threshold ( $C_T$ ). Bar graph shows mean fold change from control with nanoplastic addition ( $\Delta\Delta C_T$ ). Means are from quintuplicate independent reactions (SEM shown). \*\*\*\*p < 0.0001 from one-way ANOVA with Tukey's post-hoc test.

D) Representative surface plasmon resonance (SPR) sensorgrams with full length  $\alpha$ -synuclein (1-140, left panel), truncated 36-140 (middle panel), or 60-140 (right panel), with a range of nanoplastic contaminants in solution. Sensorgrams are globally fit to heterogeneous ligand models repeated in triplicate for each protein variant. Average  $K_d$  and  $X^2$  values (1-140, full length protein), or estimated values (low confidence  $X^2$  for the truncated proteins), are shown from three independent array runs (SEM indicated).

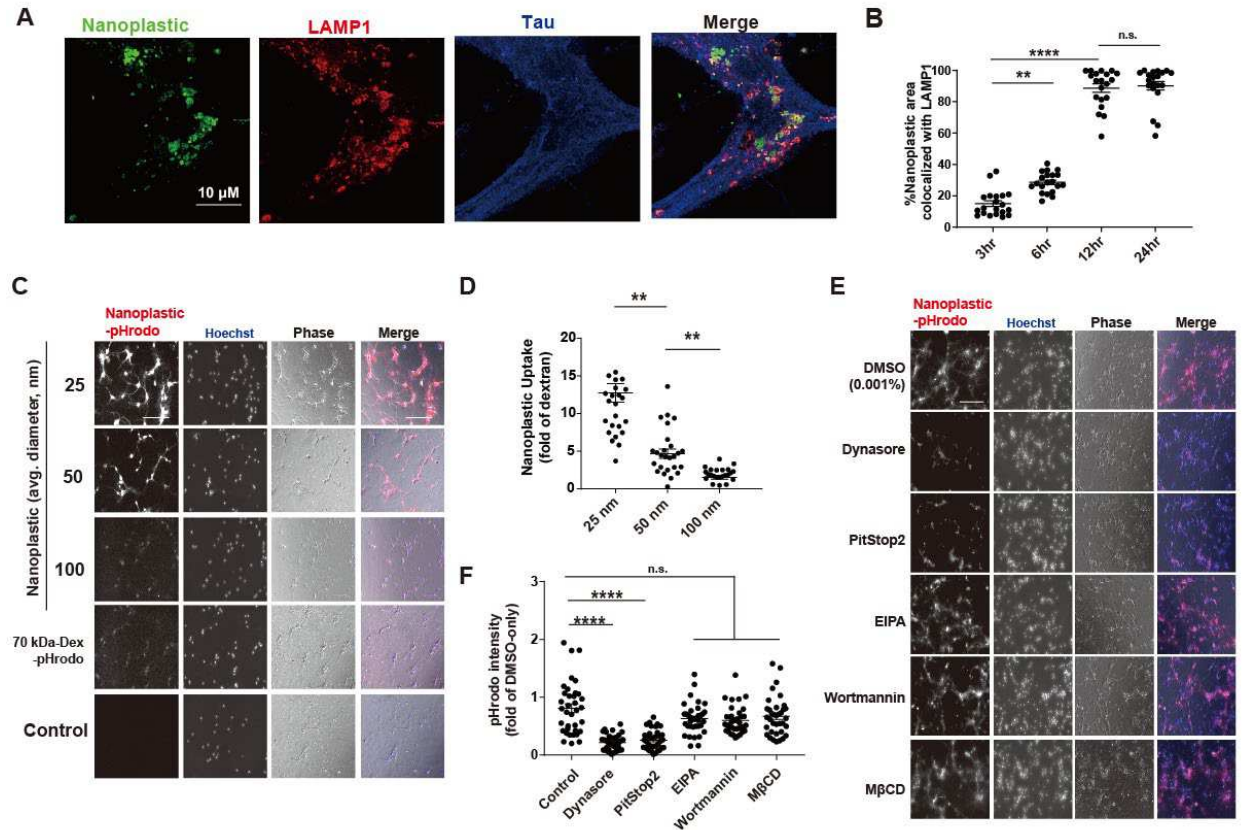


**Fig 4. Primary mouse hippocampal neurons endocytose nanoplastics through a dynamin-dependent process.**

- A) Representative Airyscan images from mouse primary hippocampal neurons (DIV 7) treated with FITC-labeled (green) nanoplastics (1 nM) for 12 hrs. Neurons were co-immunostained for tau (blue) and the lysosome marker LAMP1 (red). Scale bar, 10  $\mu$ m.
- B) Quantification of the percentage of FITC-positive areas (i.e., nanoplastic) in the Airyscan images co-localized with LAMP1. Each dot in the graph represents the mean value of co-localization found within one isolated cell, with at least 20 cells analyzed per group from three independent experiments. Representative images from this analysis are in Fig. S8.
- C) Nanoplastics particles of different diameters (pHrodo-Red, Table S1), or 70kDa-dextran (pHrodo-Red labeled), were added (10  $\mu$ g per mL) to mouse hippocampal neurons (DIV 7) for 2 hrs. Representative widefield fluorescence images are shown with phase-contrast overlays (blue and gray in merges, respectively).
- D) Quantification of plastic particle uptake, normalized as a fold of pHrodo-Red fluorescent intensity from control pHrodo-70 kDa-dextran. Each dot represents the mean value of one image analyzed from three independent neuronal cultures.
- E) Primary neurons treated with vehicle (0.001% DMSO) or the indicated endocytosis inhibitor for 20 min prior to the addition of 1 nM of pHrodo-Red nanoplastic particles for 2

hours prior to imaging. Inhibitors did not affect lysosomal acidification (Fig. S9). Hoechst and phase-contrast overlays (blue and gray in merge, respectively) are shown.

- F) Uptake of nanoplastic particles calculated as a fold of pHrodo-Red fluorescent intensity from DMSO-only treatment. Each dot represents the mean value of one image analyzed from three independent neuronal cultures.

All scale bars, 200  $\mu\text{m}$ . In panel B,D and F, black bars show group means (SEM indicated) with significance assessed by one-way ANOVA and Tukey's post hoc test. \*\* $p < 0.01$ , \*\*\*\* $p < 0.001$ , and n.s. is not significant.

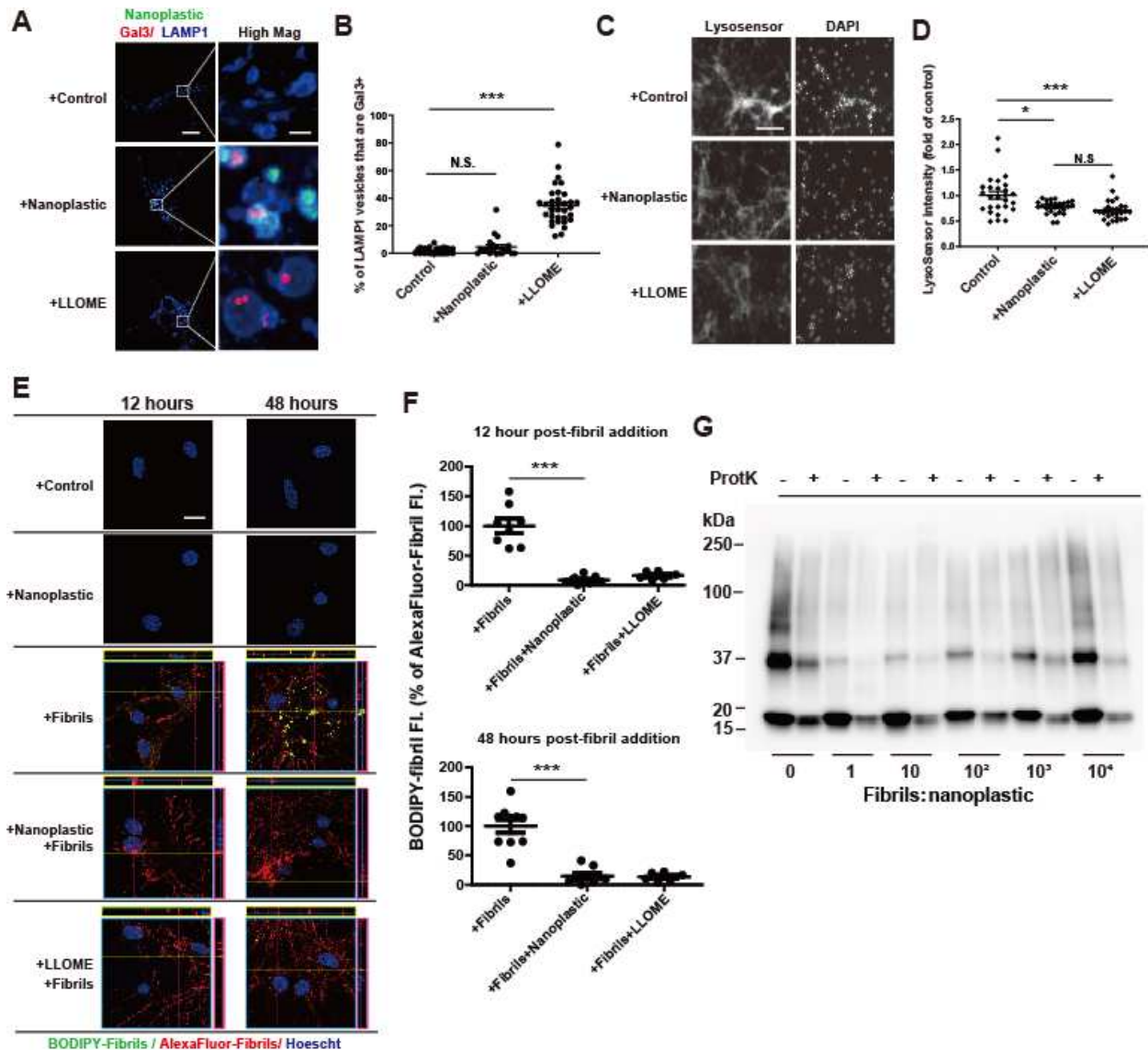


**Fig. 5. Anionic nanoplastics cause mild lysosomal impairment in neurons and attenuate the degradation of exogenous  $\alpha$ -synuclein fibrils.**

- A) Representative Airyscan images of neurons (DIV 7) treated with FITC-labeled nanoplasmic (1 nM), or 1mM L-leucyl-L-leucine methyl ester (LLOME) for 24 hours before immunostaining for galectin3 (Gal3, red) and LAMP1 (blue). Scale bar, 10  $\mu$ m, and 1  $\mu$ m for “High Mag”. B) Colocalization between Gal3 and LAMP1 in vesicles. Each dot represents the mean value from one cell analyzed of at least 20 cells from three independent experiments.
- C) Representative fluorescence images of live (DIV 7) neurons, first treated with nanoplasmic (1 nM) or LLOME (1 mM) for 24 hours, and then stained with 1  $\mu$ M LysoSensor (green) for 20 minutes, washed, and stained with Hoescht dye. Scale bar, 200  $\mu$ m. D) Quantification of relative LysoSensor green signal. Twenty-seven images



from three independent experiments were quantified for each condition, with each dot representing results from one image.

- E) Representative Airyscan images of primary neurons (DIV 7) treated with nanoplastic (1 nM),  $\alpha$ -synuclein fibrils (66.7 pM, 1:3 BODIPY-fibrils to AlexaFluor-647-fibrils), or LLOME (1mM) for the indicated time (12 or 48 hours). Orthogonal views of sequential Z-stacks are shown. Pink box=y,z plane; Yellow=x,z plane. Scale bar, 10  $\mu$ m. F) BODIPY-signal (yellow) is calculated as a percentage of total AlexaFluor-647 fibril signal, representing normalized degraded  $\alpha$ -synuclein fibrils. Each dot represents the mean analysis of one image, from three independent experiments, with at least 25 cells analyzed per group.
- G) Representative immunoblot of denatured total  $\alpha$ -synuclein products before and after partial proteinase K digestion, using  $\alpha$ -synuclein antibody MJFR1.

In panels B,D, and F, black bars show group means (SEM). \*\* is  $p < 0.01$ , \*\*\*  $p < 0.005$ , from one-way ANOVA with Tukey's post hoc test.

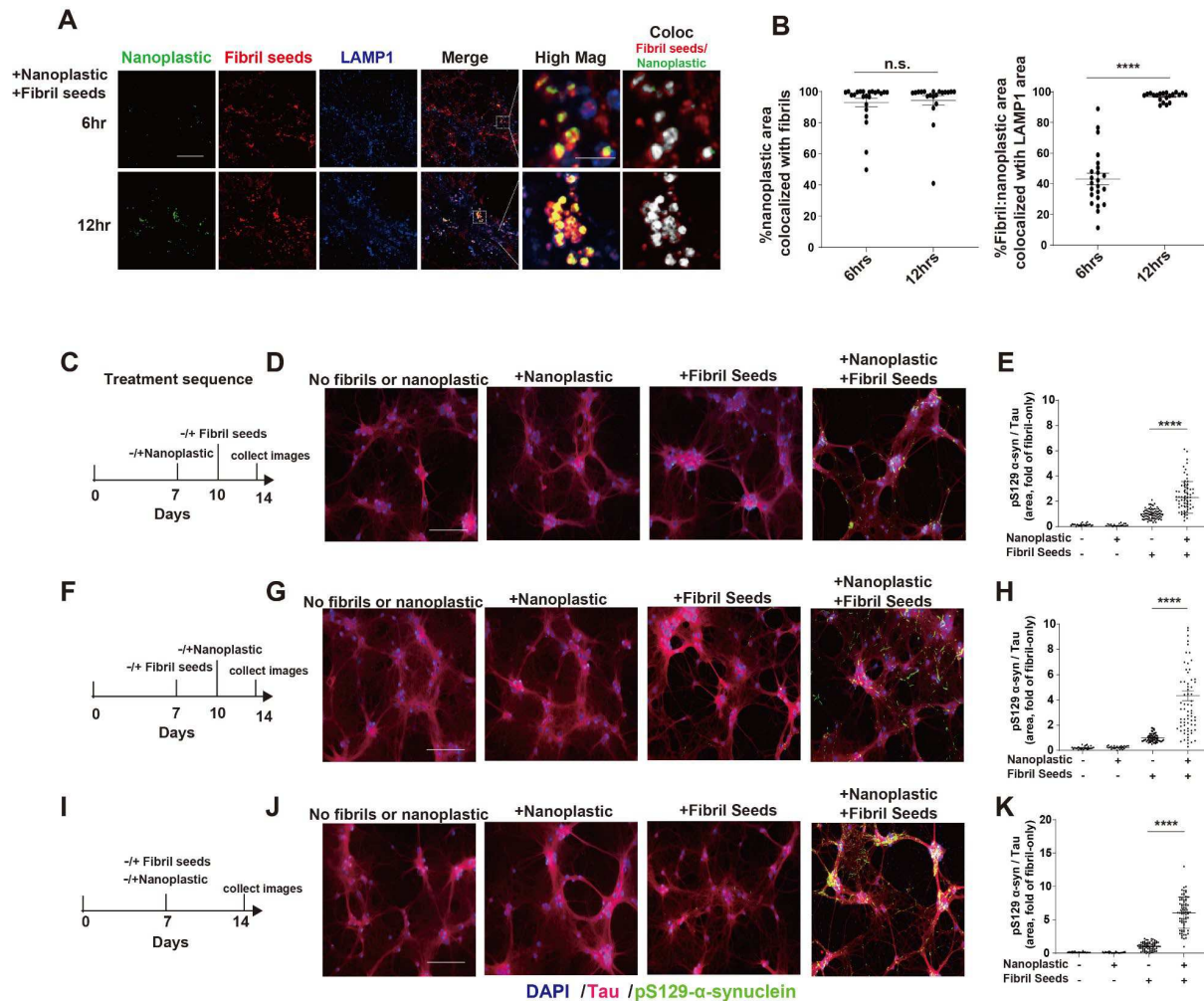


**Fig. 6. Anionic nanoplastic particles colocalize with  $\alpha$ -synuclein fibrils in lysosomes and accelerate pS129- $\alpha$ -synuclein inclusion formation in neurons.**

- A) Representative Airyscan images from mouse primary hippocampal neurons (DIV 7) exposed to both FITC-labeled nanoplastics (1 nM) and Alexa-647-labeled human  $\alpha$ -synuclein fibrils (66.7 pM). Fibrils and nanoplastic particles were not mixed prior to addition to the cell culture media. Neurons were immuno-stained at indicated time points. Colocalized pixels are shown in “High Mag” in greyscale. Scale bar, 10  $\mu$ m and 1  $\mu$ m for “High Mag”. Images from fibrils or nanoplastics at different concentrations individually added are in Fig S10.
- B) Column graphs showing the quantification of the percentage of nanoplastic area co-positive with fibrils over time (left panel), and the percentage of nanoplastic-fibril double positive areas that are co-localized with LAMP1 signal (right panel).
- C) Timeline for the sequential addition of unlabeled nanoplastic (1 nM) and then unlabeled fibrils (66.7 pM), and D) representative immunofluorescence for tau and pS129- $\alpha$ -synuclein. E) Quantification pS129- $\alpha$ -synuclein area occupying tau-positive area.

- F) Reversed addition of particles, first with fibril seeds (DIV 7) and then nanoplastic (DIV14), with G) representative immunofluorescence and H) quantification of pS129- $\alpha$ -synuclein area.
- I) Simultaneous addition of both fibril seeds and nanoplastic at DIV 7, with J) representative immunofluorescence and K) quantification of pS129- $\alpha$ -synuclein area.

All timelines included the independent analysis of no fibrils or nanoplastic added (first column in each graph), as well as the effects of each particle on their own (second and third columns in each graph).

Scale bars, 200  $\mu$ m. Each dot in each column graphs represents the mean value of one cell analyzed from at least 20 cells per condition from three independent experiments. Black bars show group means (SEM), with significance assessed by one-way ANOVA with Tukey's post hoc test. \*\*\*\* $p < 0.0001$ .

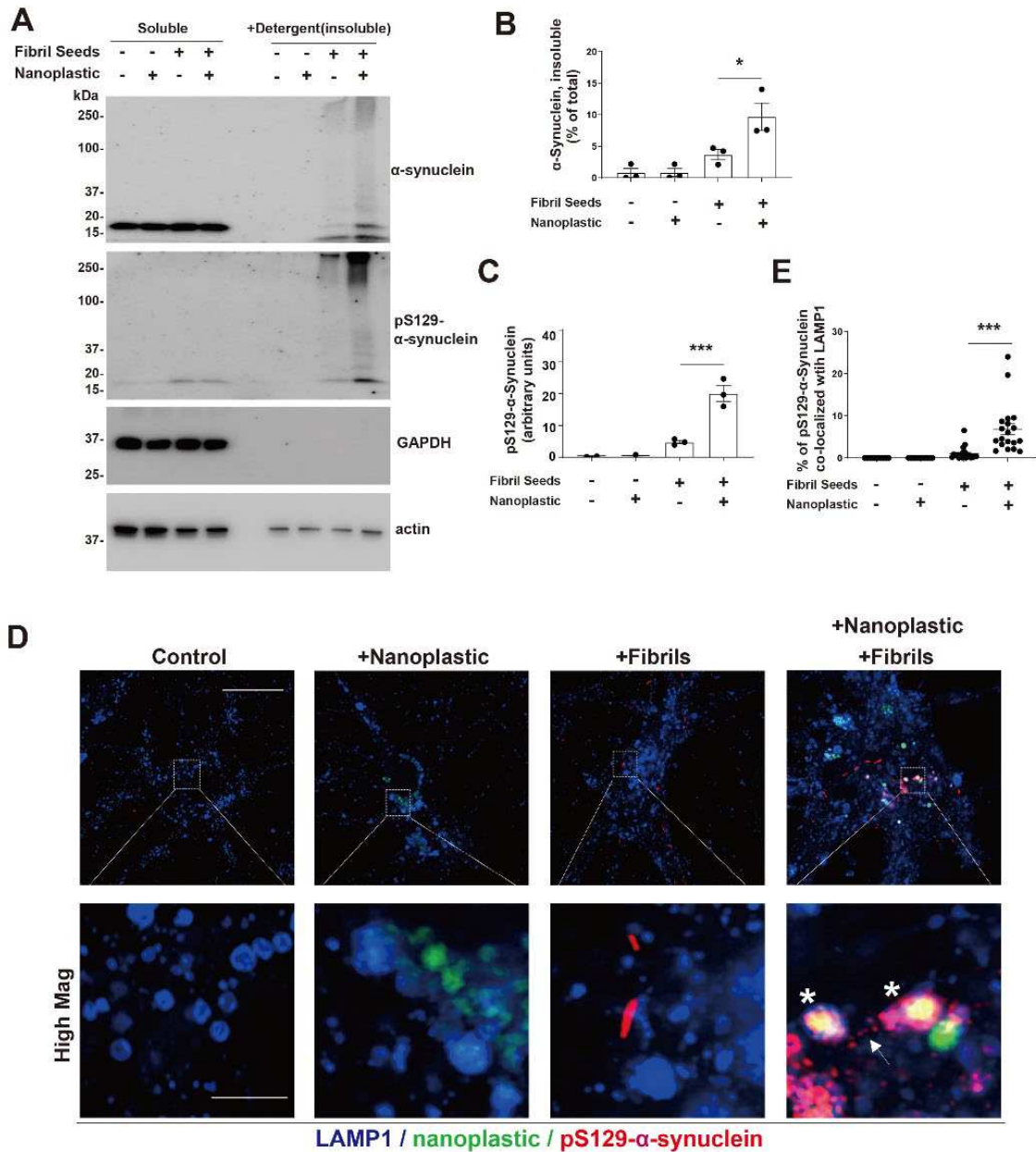


**Fig 7. Nanoplastic contaminants enhance the formation of insoluble pS129- $\alpha$ -synuclein at the lysosome in neurons.**

- A) Primary mouse hippocampal neurons (DIV 7) from non-transgenic mice were treated with 1 nM unlabeled nanoplastics together with  $\alpha$ -synuclein fibril seeds as indicated. Cells were lysed (DIV 14) and proteins separated into soluble fractions and SDS-solubilized (i.e., insoluble) fractions, followed by SDS-PAGE and immunoblotting.
- B) Quantification of the percent of  $\alpha$ -synuclein measured in the insoluble fraction, or C) the relative amount of pS129- $\alpha$ -synuclein in the insoluble fraction. Each dot in the columns represents the analysis of an independent lysate from an independent experiment.

- D) Representative Airyscan images of neurons stained for LAMP1 (blue), nanoplastic (green), and pS129- $\alpha$ -synuclein (red). Asterisks highlight vesicles triple-positive for these markers. Scale bars, 10  $\mu$ m, and 1  $\mu$ m for “High Mag”.
- E) Quantification of the percentage of pS129- $\alpha$ -synuclein signal that overlaps with LAMP1 in the indicated conditions from panel D. Each dot in the column graphs represents the mean value of one cell analyzed from at least 20 cells from three independent experiments.

Bars and lines in panels B,C, and E show group means (SEM), with significance assessed by one-way ANOVA and Tukey's post hoc test. \* $p < 0.05$  and \*\*\* $p < 0.001$ .

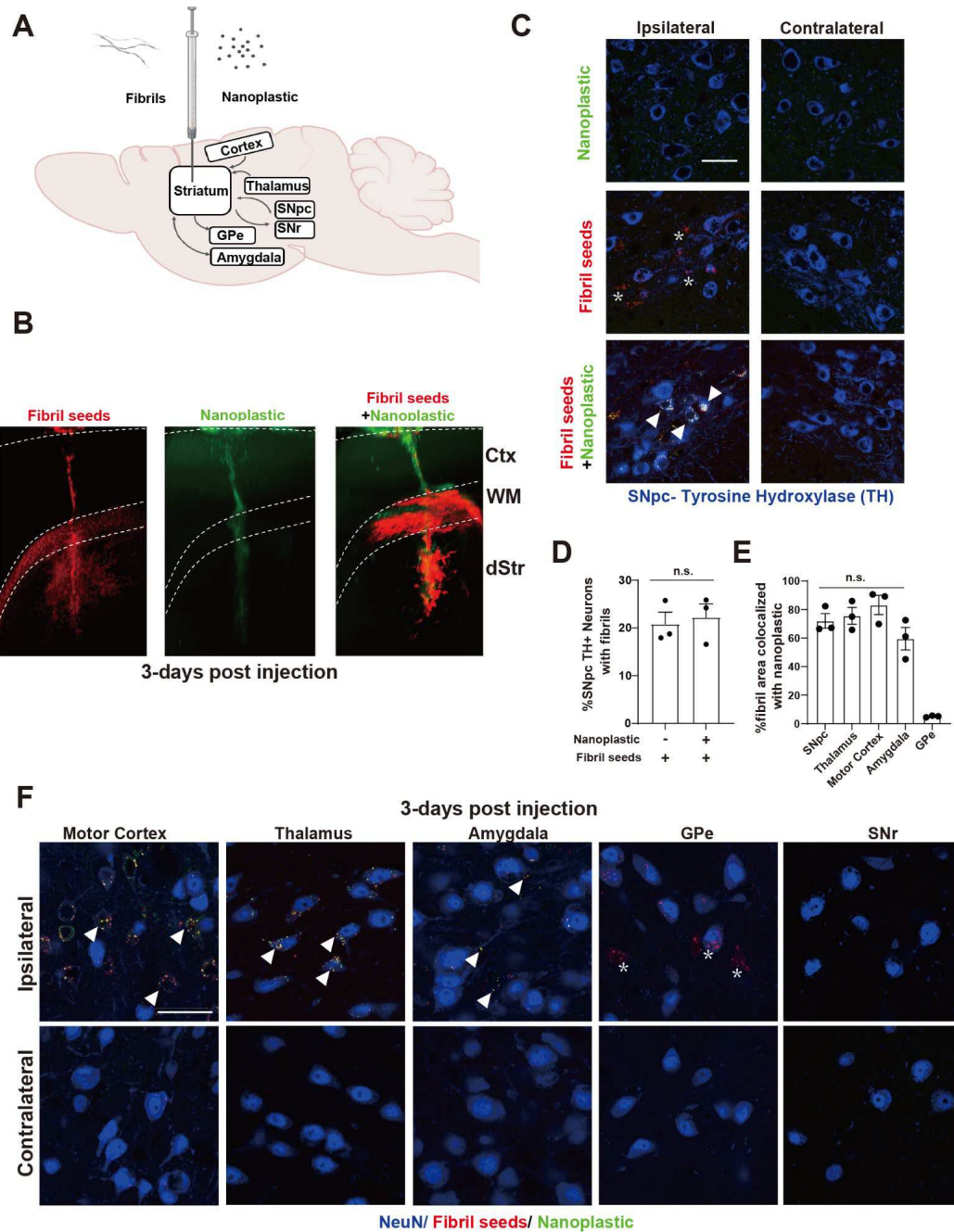


**Fig. 8. Anionic nanoplastics contaminants traffic with  $\alpha$ -synuclein fibrils along retrograde projections and accumulate in neuronal bodies.**

A) Depiction of ~P90 male (non-transgenic) mice injected unilaterally in the dorsal striatum with 15  $\mu$ g of FITC-conjugated nanoplastic, or 4.5  $\mu$ g Alexa-647 labeled human  $\alpha$ -synuclein fibrils, or the injection of these particles together. Anterograde projections from the injection site include the globus pallidus (GPe) and substantia nigra pars reticulata

(SNr), whereas retrograde projection targets include the amygdala, motor cortex, thalamus, and substantia nigra pars compacta (SNpc).

- B) Representative light-sheet microscopy of mouse brain, analyzed 3 days after injections, with  $\alpha$ -synuclein fibril-only (red), nanoplastic-only (green), or co-particle injections. The cortex (Ctx), corpus callosum (WM), and dorsal striatum (dStr) layers are indicated.
- C) Representative Airyscan images of dopaminergic cells in the SNpc, with arrowheads indicating cells with vesicles filled with both fibrils and nanoplastics (white signal). Asterisks show neurons from fibril-only injections. Results are representative of three mice injected per group. Scale bar, 50  $\mu$ m.
- D) Column graph showing the mean proportion of dopaminergic neurons positive for fibrils with or without nanoplastic co-injection. E) Column graph showing the proportion of fibril-nanoplastic co-positivity is similar across retrograde-targeted brain regions, with the exception of the GPe (anterograde from injection site). Each dot represents the mean of sections analyzed through one separate animal, one-way ANOVA with Tukey's post-hoc test were used.
- F) Representative Airyscan images of neurons analyzed in panel E, with arrow-heads highlighting neurons filled with vesicles co-labeled (yellow) with nanoplastic and fibrils, whereas asterisks highlight neurons filled with only fibrils (GPe). No fibrils or nanoplastics were detected in the SNr. Scale bar, 50  $\mu$ m.

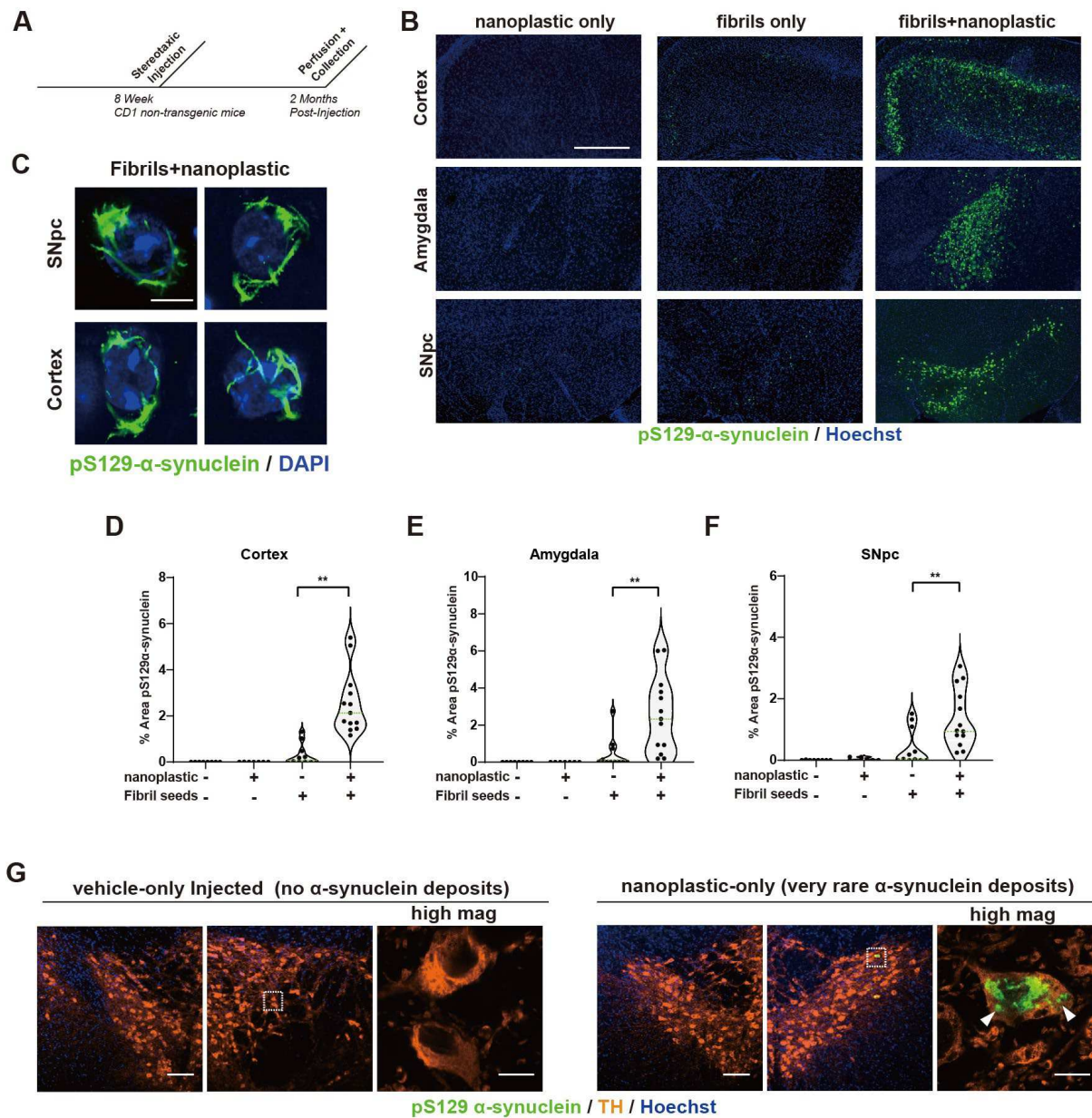


**Fig. 9. Anionic nanoplastic contaminants in the brain synergize with  $\alpha$ -synuclein fibrils to increase the deposition of pathology in the cortex, amygdala, and substantia nigra in non-transgenic mice.**

- A) Timeline for the injection of adult (non-transgenic) male mice with control saline (N=8 mice), or 4.5  $\mu$ g of unlabeled  $\alpha$ -synuclein fibrils (N=12 mice), or 4.5  $\mu$ g of unlabeled  $\alpha$ -synuclein fibrils combined with 15  $\mu$ g unlabeled nanoplastic (N=12 mice).
- B) Representative immunofluorescence staining of  $\alpha$ -synuclein pathology (pS129- $\alpha$ -synuclein, green) in the indicated brain region two months after injections Scale bar, 0.5 mm.



- C) Representative high-magnification Airyscan images of pS129- $\alpha$ -synuclein staining inside of dopaminergic neurons (SNpc) or pyramidal neurons in the motor cortex (cortex). Scale bar, 10  $\mu$ m.
- D) Violin plots showing the distributed  $\alpha$ -synuclein inclusion burden (pS129- $\alpha$ -synuclein area in each image) in ipsilateral cortex, E) amygdala, and F) SNpc. Mean percent areas of the indicated brain nuclei occupied by pS129- $\alpha$ -synuclein staining are plotted, where each dot represents the analysis of all sections through the respective brain region of one animal. \*\* $p < 0.01$ , Mann-Whitney U test.
- G) Two months after nanoplastic-only injections, three of ten mice demonstrated robust but isolated  $\alpha$ -synuclein inclusions (green) in dopaminergic neurons in the SNpc, suggesting nanoplastic on its own can induce *de novo* mature inclusions. Bounding boxes are magnified to highlight these inclusions (arrowheads). Scale bars, 100  $\mu$ m and 10  $\mu$ m for “high mag”.

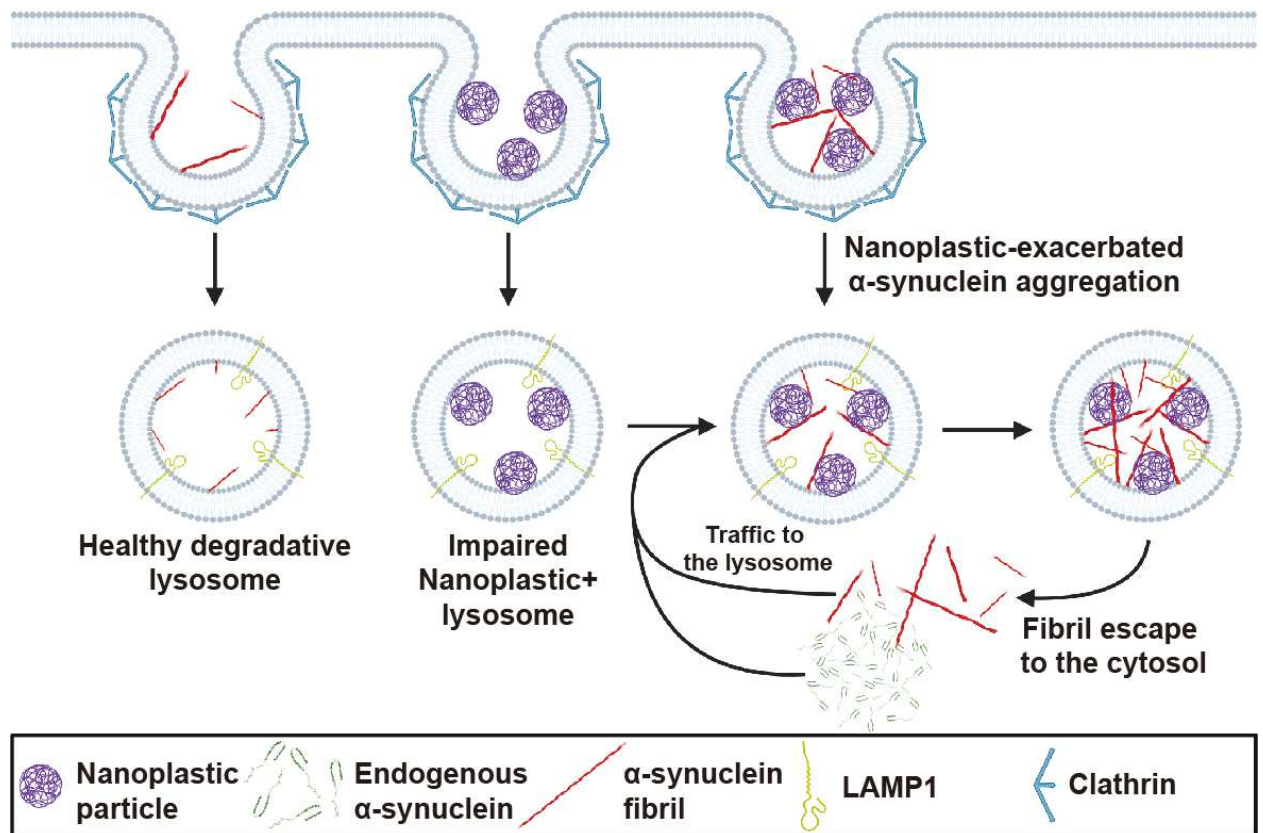


**Fig. 10. Hypothetical model for the pathological interaction between  $\alpha$ -synuclein and nanoplastic contaminants in neurons.**

Nanoparticles that have the intrinsic capacity to disrupt and cross the blood brain barrier, such as small charged polystyrene particles, may come into contact with neurons that express high levels of  $\alpha$ -synuclein and can harbor aggregates in disease. Peripheral cells susceptible to  $\alpha$ -synuclein aggregation and outside of the blood brain barrier (e.g., vagal neurons) may also come into contact with nanoplastic contaminants. Both  $\alpha$ -synuclein fibrils and nanoplastics can enter the endolysosomal compartment in neurons through a clathrin-dependent endocytosis process. A healthy lysosome might fully degrade an  $\alpha$ -synuclein aggregate. However, if a lysosome is impaired by nanoplastic particles,  $\alpha$ -synuclein aggregates might not degrade and endogenous  $\alpha$ -synuclein trafficked to the lysosome may inadvertently spur the formation of new  $\alpha$ -synuclein fibrils through the potent pro-aggregation catalytic action of nanoplastics. This feedforward pathway highlights a two part proposed mechanism whereby nanoplastic contaminants may accelerate the formation of misfolded  $\alpha$ -synuclein in the endolysosome compartment and simultaneously impair the degradative action of the organelles (i.e., lysosomes) primarily responsible for their clearance.

## Supplementary Materials for

# Anionic Nanoplastic Contaminants Promote Parkinson's Disease-Associated $\alpha$ -Synuclein Aggregation

Zhiyong Liu<sup>\*1</sup>, Arpine Sokratian<sup>\*1</sup>, Addison M. Duda<sup>2</sup>, Enquan Xu<sup>1</sup>, Christina Stanhope<sup>1</sup>, Amber Fu<sup>1</sup>, Samuel Strader<sup>1</sup>, Huizhong Li<sup>1</sup>, Yuan Yuan<sup>1</sup>, Benjamin G. Bobay<sup>2</sup>, Joana Sipe<sup>3</sup>, Ketty Bai<sup>1</sup>, Iben Lundgaard<sup>4,5</sup>, Na Liu<sup>4,5</sup>, Belinda Hernandez<sup>6</sup>, Catherine Bowes Rickman<sup>6</sup>, Sara E Miller<sup>7</sup>, Andrew West<sup>1\*\*</sup>

**\*\*Corresponding author: Email: [andrew.west@duke.edu](mailto:andrew.west@duke.edu)**

Figs. S1 to S14

Captions for Figs. S1 to S14

Table S1

Supplemental Methods

Captions for Auxiliary Supplemental Materials

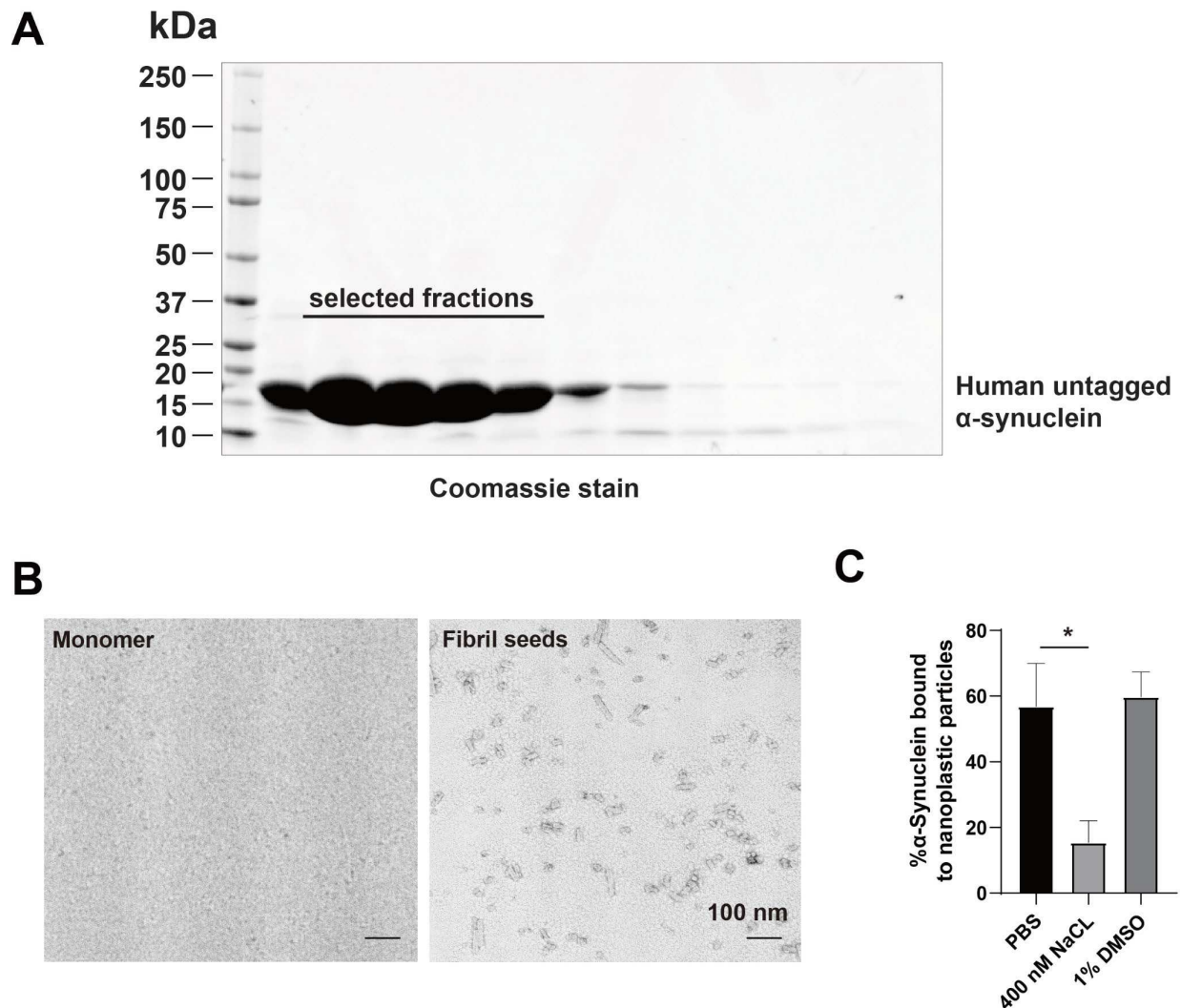


**Fig. S1. Validation of monomeric and  $\alpha$ -synuclein fibril seeds.**

- A) Representative SDS-PAGE and Coomassie stain of selected eluted fractions from boiled bacterial lysates with untagged human  $\alpha$ -synuclein protein processed through HiPrep Q HP 16/10 columns.
- B) Representative negative stain electron microscopy of purified  $\alpha$ -synuclein monomer and fibril seeds (generated by sonication of full length fibrils to the terminal stage). Monomer protein was screened via TEM to detect possible oligomers or larger aggregates. Processed sonicated fibril seed length was consistent with light-scattering diameter estimations for the stumpy fibril particles. Very small stumpy fibril particles are exceptionally stable under physiological conditions according to past analyses (24). Scale bar, 100 nm.
- C) Group analysis of the propensity of  $\alpha$ -synuclein fibrils to bind nanoplastic particles after 30 min RTe incubation in PBS, or PBS supplemented with 400 nM NaCl (i.e., high-salt), or 1% DMSO in water, measured by light-scatter. Each group mean (column) represents an average of 10 acquisitions with error bars indicating SEM.



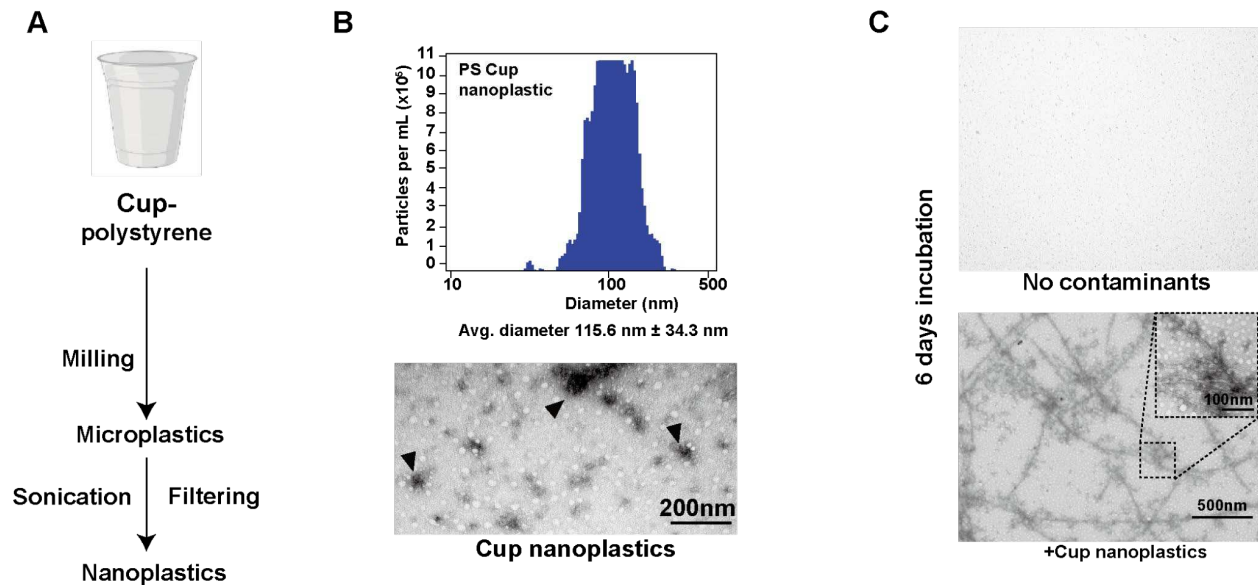


**Fig. S2. Cup-abraded environmental polystyrene nanoplastic in  $\alpha$ -synuclein aggregation.**

- A) Workflow of nanoplastic production from plastic cups. Microplastics from polystyrene plastic cups generated by grinding were sonicated to break larger aggregates and then filtered (0.2-micron) to enrich nanoplastic particles.
- B) Representative light scattering plot and TEM of abraded nanoplastics contaminants from a polystyrene cup. Arrowheads indicate particles with sizes consistent with light scattering analysis (upper panel, blue). Scale bar, 200 nm.
- C) Representative TEM images of 70  $\mu$ M human  $\alpha$ -synuclein (monomeric) shaken at 37  $^{\circ}$ C in absence (top) or presence of 1 nM (estimated, Zeta nanoparticle tracking analysis) polystyrene cup nanoplastic contaminants for 6 days. Bounding boxes show magnified representative fibrils and nanoplastic-tethered particle interactions. Bars = 500 nm and 100 nm for magnified inset.

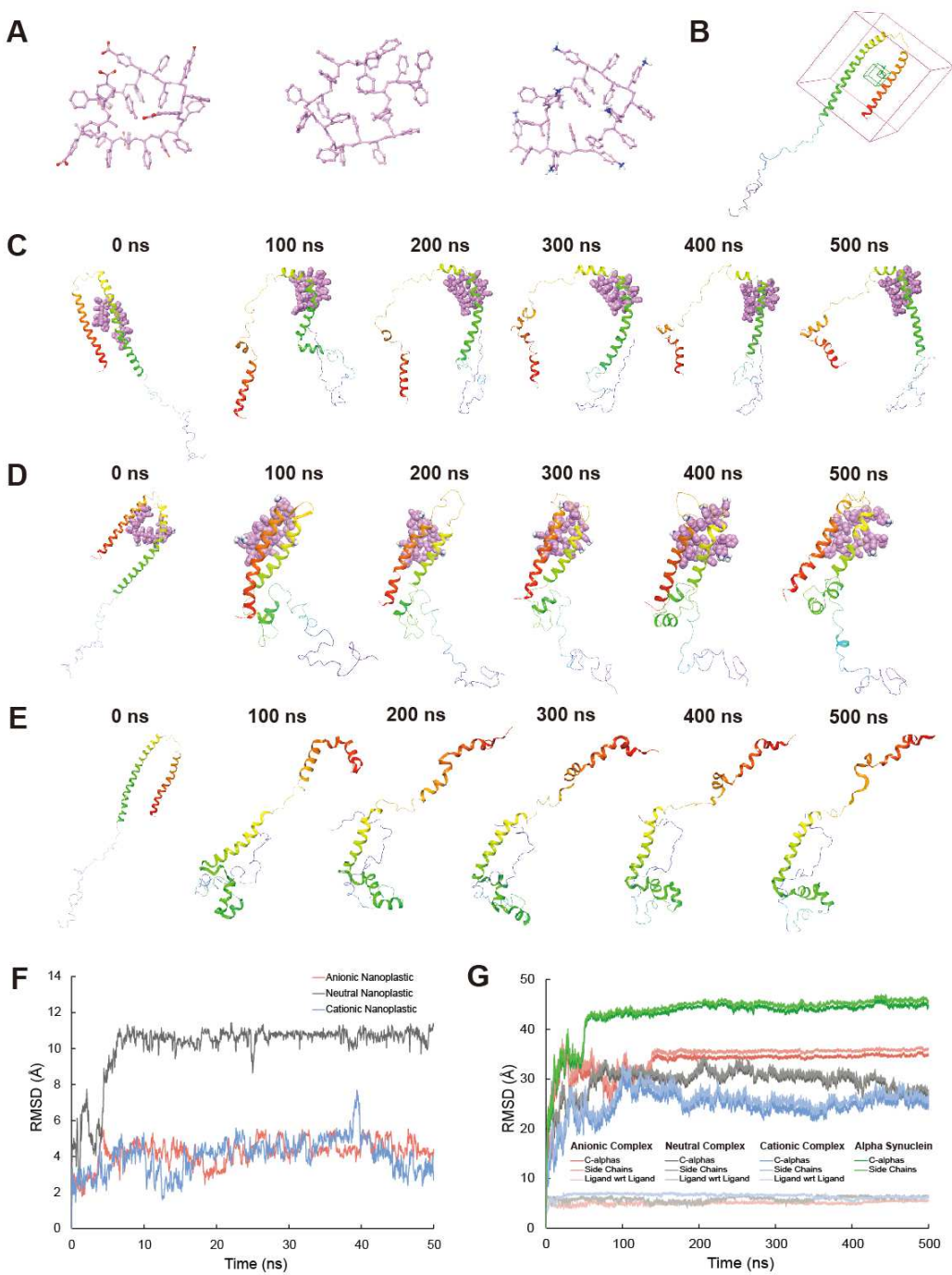
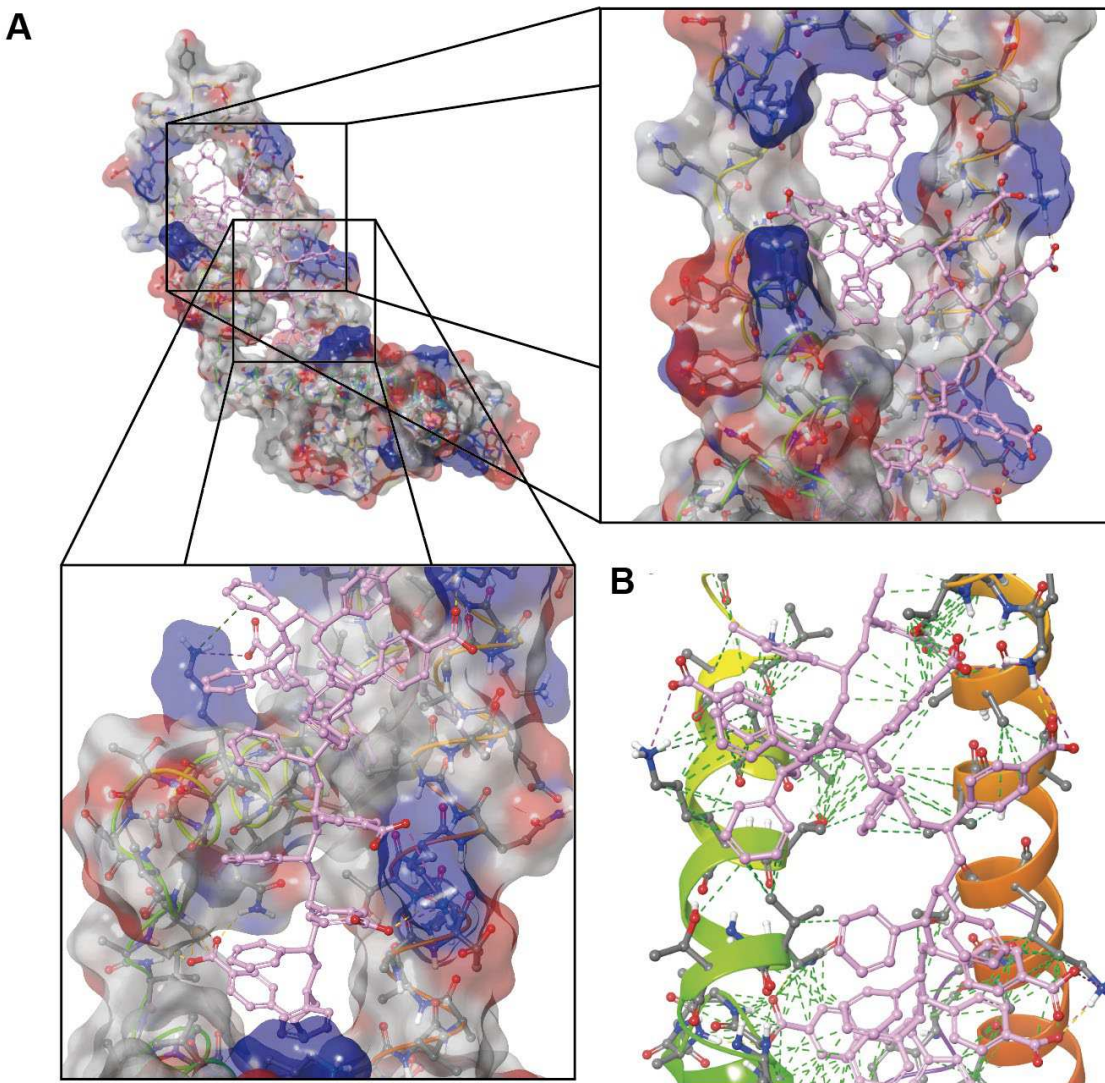


**Fig. S3. Structures and molecular dynamics time frames, ligand RMSDs, and complex RMSDs that highlight the differential effects of anionic nanoplastics on  $\alpha$ -synuclein folding.**

A) Representative frames of converged geometry-optimized anionic, neutral, and cationic nanoplastics, left to right (ball-and-stick, only polar hydrogens shown; white = hydrogen, pink = carbon, blue = nitrogen, red = oxygen).

- B) Representation of docking box (purple, 46 Å) used for the Induced Fit Docking method to introduce nanoplastics to  $\alpha$ -synuclein monomeric protein.
- C) Snapshots of neutral nanoplastic and  $\alpha$ -synuclein (ribbon colored by residue index) complex, D) cationic nanoplastic and  $\alpha$ -synuclein complex, or E)  $\alpha$ -synuclein alone across MD simulations, at 100 ns intervals. Nanoplastics depicted as space fill, showing polar hydrogens only; white = hydrogen, pink = carbon, blue = nitrogen.  $\alpha$ -Synuclein is depicted in ribbons and colored by residue index. Of note, neutral and cationic nanoplastics have different associations, fewer contacts, and weaker interactions with  $\alpha$ -synuclein as compared to anionic nanoplastic.
- F) RMSD plots of MD-simulated nanoplastics confirming simulations converge within 10 ns. RMSDs were calculated for heavy atoms of each ligand using frame 1 as a reference.
- G) RMSD plots of nanoplastic/ $\alpha$ -synuclein complexes and  $\alpha$ -synuclein alone confirming simulations converge within 200 ns. RMSDs were calculated for indicated atoms of the complexes and  $\alpha$ -synuclein alone using frame 1 as a reference. C-alphas is the RMSD of only the  $\alpha$ -carbons of  $\alpha$ -synuclein's backbone, Side Chains is the RMSD of only the heavy atoms of the residue side chains. Ligand with respect to (wrt) Ligand is the RMSD calculated for the heavy atoms of the nanoplastic in the  $\alpha$ -synuclein complex. Simulations converge within 200 ns.

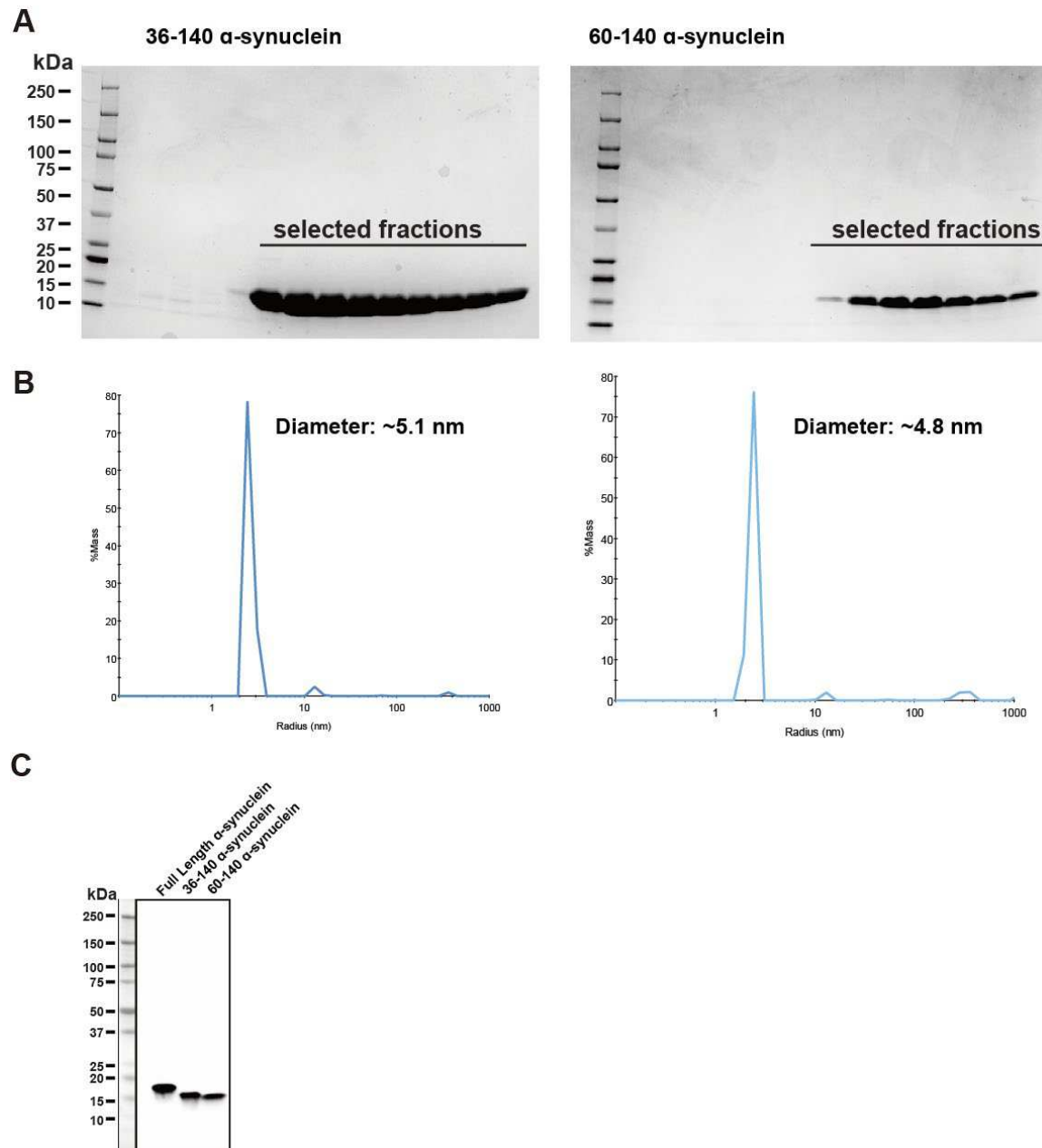




**Fig. S4. Anionic nanoplastic complex molecular surface and Van der Waals (VDW) contacts highlight water displacement and tight association.**

- A) Representative frame of anionic nanoplastic and  $\alpha$ -synuclein complex, with individual blow ups highlighting plastic-protein surface interactions. Carboxylates associate with areas of positively charged densities to form strong polar bonds while the hydrophobic backbone of the nanoplastic occupies regions rich with nonpolar residues. The surface of  $\alpha$ -synuclein bound to anionic nanoplastic becomes free of solvent water. Anionic nanoplastic is depicted as ball-and-stick, showing polar hydrogens only; pink = carbon, red = oxygen.  $\alpha$ -synuclein backbone depicted as cartoon ribbon colored by residue index; residues are ball-and-stick showing polar hydrogens only; white = hydrogen, grey = carbon, blue = nitrogen, red = oxygen; 50 % transparent molecular surface colored by residue charge, blue = positive, grey = neutral, red = negative

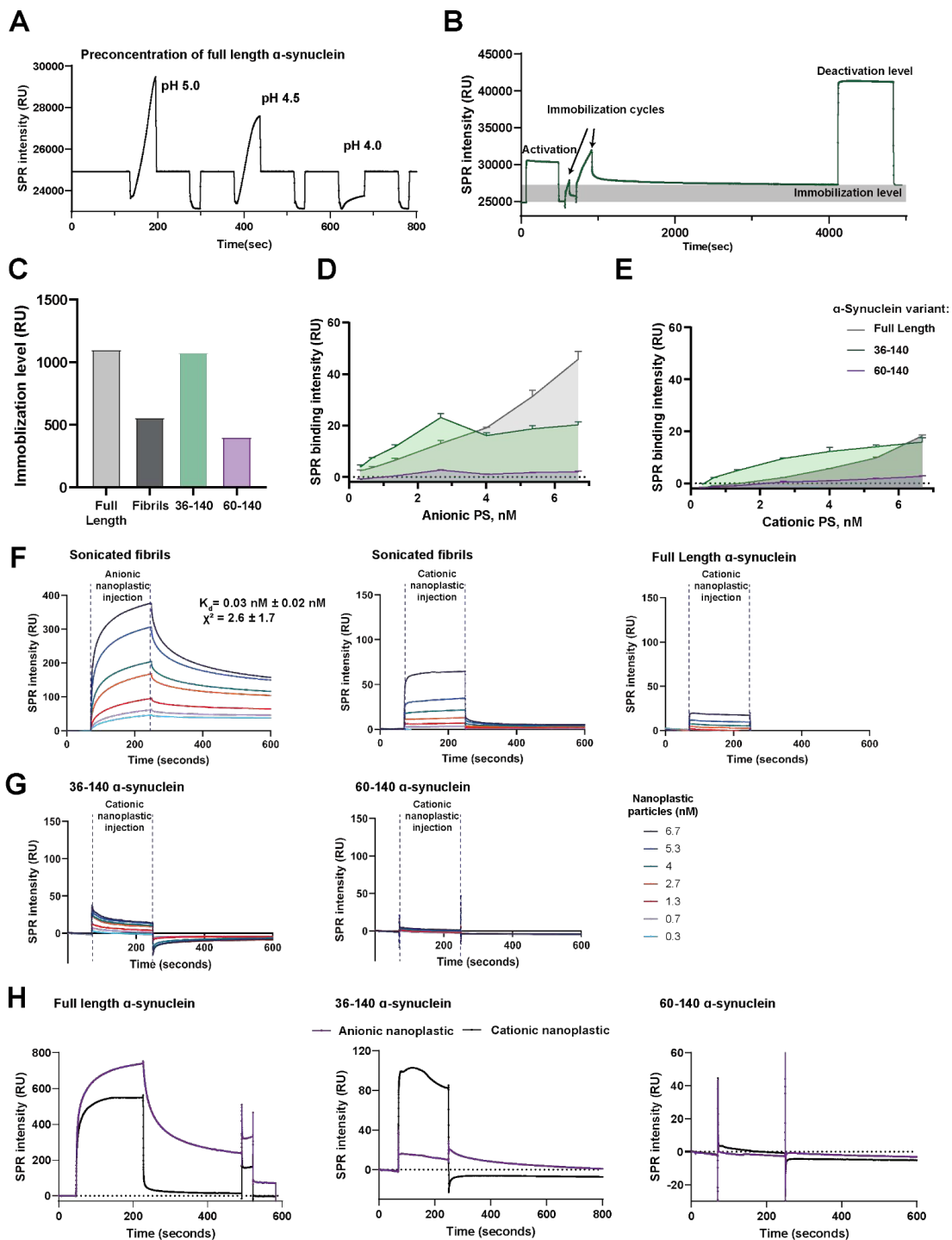
B) A representative web of Van der Waals (VDW) contacts shows tight association of the anionic plastic in the protein complex. Shown is a matched frame (as in Figure 2D), but now indicating VDW interactions. Anionic nanoplastic forms a web of good VDW contacts with  $\alpha$ -synuclein. Green dashed lines represent good VDW contacts, whereas orange dashed lines represent rough VDW contacts, and red designates bad VDW contacts.



**Fig. S5. Validation of N-term truncated  $\alpha$ -synuclein recombinant proteins.**

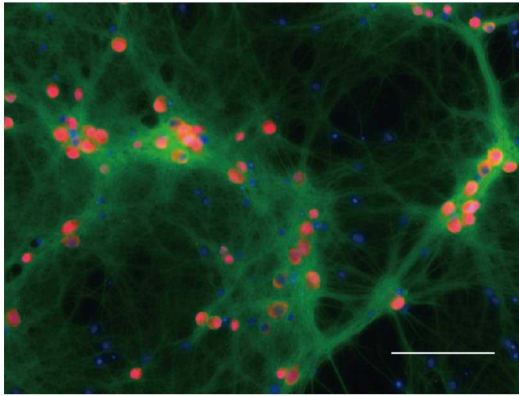
- A) N-truncated  $\alpha$ -synuclein variants 36-140 and 60-140 were prepared similarly to full length protein. Representative SDS-PAGE and Coomassie stain analysis of eluted fractions demonstrate pure protein preparations selected for further purification and concentration. Variant 36-140 shows lower molecular weight as expected, with a negative charge of -11.2 at pH 7.5, while 60-140 has a negative charge of -12.2 at pH 7.5.
- B) Representative dynamic light scattering (DLS) histograms of purified 36-140 (left) and 60-140 (right), plotted relative to the mass distribution-predicted molecular weight, demonstrating monomeric (i.e., non-aggregated) protein.

C) Representative immunoblot to detect (~1 ng loaded each lane) recombinant full length (1-140) and truncated variants (36-140 and 60-140) with the monoclonal anti- $\alpha$ -synuclein antibody MJF1R that binds nearer the C-terminus.

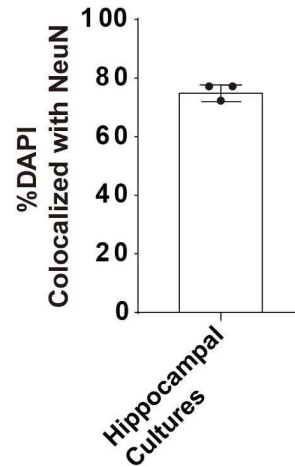


**Fig. S6.** Surface plasmon resonance analysis showing activation, immobilization, deactivation, and the necessity of negatively-charged nanoplastic for interaction with the amphipathic domain in  $\alpha$ -synuclein.

- A) A representative graph of a pre-concentration SPR sensorgram indicates the effects of immobilization pH (10 mM sodium acetate) leading to a change of the electrostatic attraction of  $\alpha$ -synuclein at the surface of the CM5 chip resulting in a spike of SPR intensity. Dilution of protein in the sodium acetate buffer at different pH allows for the identification of efficient immobilization conditions. Exemplary injections of full length  $\alpha$ -synuclein at different immobilization pH indicate the highest spike of SPR intensity at pH 5 with gradual decreases from pH 4.5 to 4.
- B) Representative SPR sensorgram of  $\alpha$ -synuclein immobilization to an SPR chip activated by 1-ethyl-3-(3-dimethylaminopropyl) carbodiimide (EDC)/N-hydroxysuccinimide (NHS), enabling amine-targeted immobilization. Deactivation with ethanolamine quenches any unreacted carboxyl groups and rids the surface of nonspecifically bound  $\alpha$ -synuclein. Increases in SPR intensity after iterative cycles of immobilization, highlighted in gray, indicates the effects of conjugation of  $\alpha$ -synuclein to the chip with 200 - 1000 RU, an index generally compatible with sensitive kinetic measurements.
- C) Columns depict final immobilization as shown in B) for full length  $\alpha$ -synuclein,  $\alpha$ -synuclein fibrils, and the two N-terminal truncated variant proteins.
- D) Group analysis histograms of changes in SPR binding intensity upon injection of anionic and E) cationic nanoplastic particles for interaction with full length  $\alpha$ -synuclein, and the truncated 36-140 and 60-140 variant proteins. The rate of binding in SPR measurements was calculated with Biacore T200 Evaluation Software as SPR RU at the end of the analyte injection, with subtracted blank reference values.
- F) Titration-based SPR curves of immobilized  $\alpha$ -synuclein fibrils with injection of nanoplastic particles demonstrates anionic (left panel), but not cationic nanoplastic, can interact tightly with  $\alpha$ -synuclein. Extracted average  $K_d$  values from three independent reactions with indicated SEM and  $X_2$ , calculated with heterogeneous analyte model fit on Biacore T200 software. Binding analyses of both fibrils (middle) and full length monomeric  $\alpha$ -synuclein protein (right panel) to cationic nanoplastic particles were marked as negative in the fitting process. While addition of cationic nanoplastic to fibrils immobilized on the chips results in spikes of intensity during injection steps, dissociation cycling leads to immediate return to the initial RU levels, indicative of weak and non-specific interaction.
- G) Binding analysis of cationic nanoplastic to 36-140 (left) and 60-140 (right)  $\alpha$ -synuclein variants measured by SPR kinetic analysis.
- H) Representative SPR sensorgrams of interactions between immobilized full length  $\alpha$ -synuclein (left), truncated 36-140 protein (middle), and truncated 60-140 protein (right) and anionic or cationic nanoplastic at 15 nM. Anionic nanoplastic particle injection shows specific association and dissociation profiles exclusively in the presence of conjugated full length  $\alpha$ -synuclein, while positively charged particles demonstrate strong associations followed by rapid dissociations that highlight weak and non-specific interactions. Truncated 36-140  $\alpha$ -synuclein shows weak association with cationic particles and no response with anionic nanoplastic. Likewise truncated 60-140 protein demonstrates no significant binding to anionic or cationic nanoplastic particles.

**A**

DAPI/Tau/NeuN

**B**

**Fig. S7. Characterization of primary neurons via tau and NeuN immunostaining shows high neuronal purity and high neuronal tau-positive process complexity.**

- A) A representative image of primary mouse hippocampal neurons used in this study, derived from post-natal (P0) CD-1 mice and cultured for at least 7 days *in vitro* (DIV 7) before treatment with nanoplastics (or fibrils) as indicated. Representative images show highly arborized and interconnected neurons. Red indicates NeuN staining that primarily localizes to the neuronal cell body, and blue labels DAPI staining primarily localized to the nucleus, and green shows tau staining distributed smoothly along neuritic processes.
- B) The ratio of Hoechst-positive to NeuN-positive cells (e.g., neurons) in cultures (from N=3 biologically independent experiments, SEM) shows a minority of non-neuronal cells in culture. The NeuN-negative cells are presumed to be primarily astrocytes that are morphologically distinct from neurons in the culture.

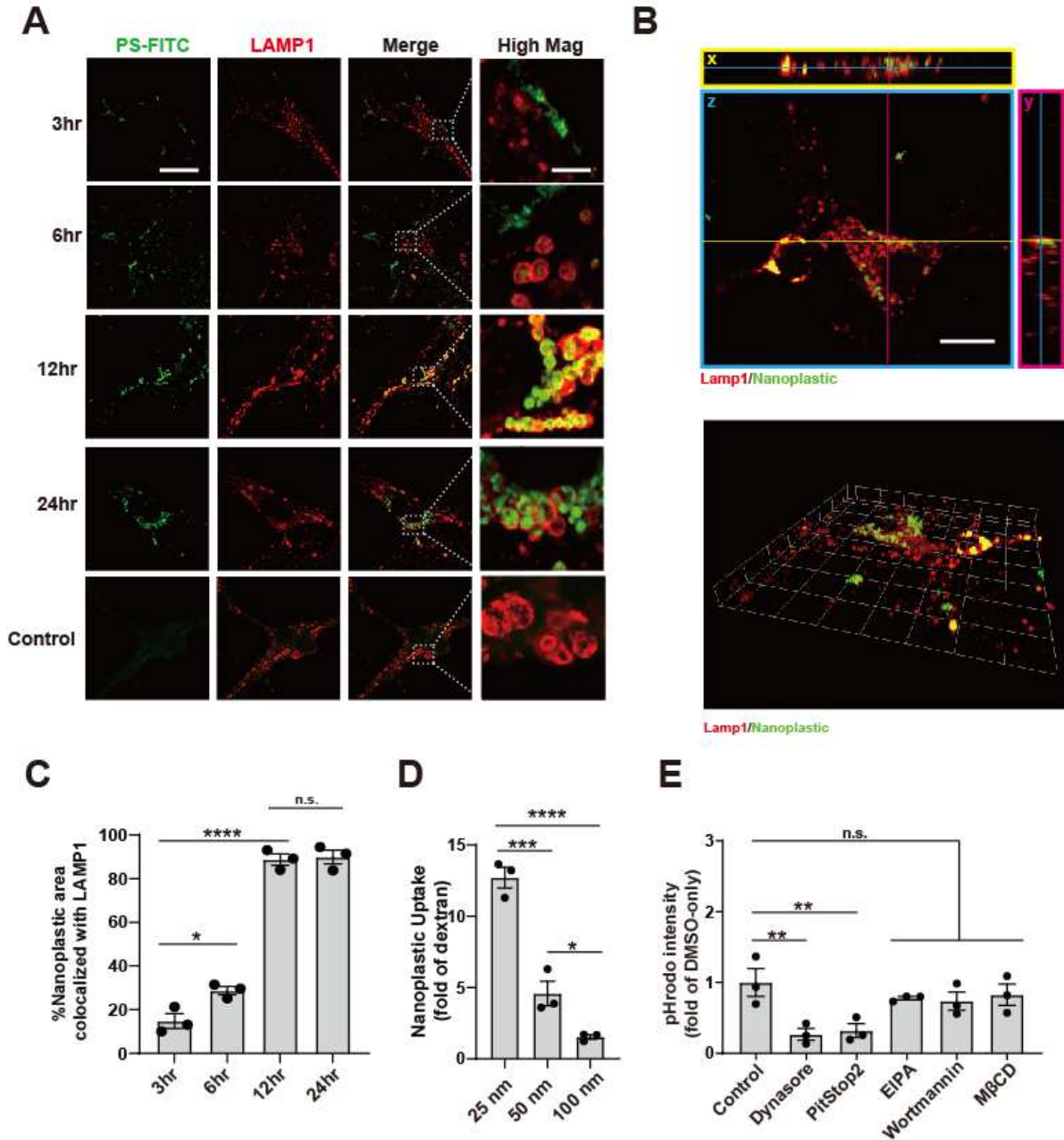


**Fig. S8. Primary mouse hippocampal neurons endocytose nanoplastics through a dynamin-dependent process.**

- A) Representative confocal Airyscan images from mouse primary hippocampal neurons (DIV 7) treated with FITC-labeled (green) nanoplastic (1 nM) for 3, 6, 12 and 24, hrs. Scale bar, 10  $\mu$ m and 1  $\mu$ m for “High Mag”.
- B) A representative Airyscan confocal image from mouse primary hippocampal neurons (DIV 7) simultaneously exposed to FITC-labeled nanoplastics. Neurons were immunostained at 24 hours after the addition of the particles. The orthogonal view (left panel) from sequential Z-stacks is shown. Pink line is the intersection of y,z; Yellow line is x,z;



Cyan line is x,y. Cyan box is the x,y plane; Pink box is the y,z plane; Yellow box is the x,z plane. Scale bar represents 10  $\mu\text{m}$ . The reconstructed 3D view is shown in the right panel.

- C) C-E) Data corresponding to main Fig. 4 panels B,D, and F are shown where each dot is the mean value from the analysis of all images from three biologically independent experiments. Each column shows the group mean (SEM). \* $p < 0.05$ , \*\* $p < 0.01$ , \*\*\*\* $p < 0.001$ , and n.s. is not significant, one-way ANOVA and Tukey's post hoc test.

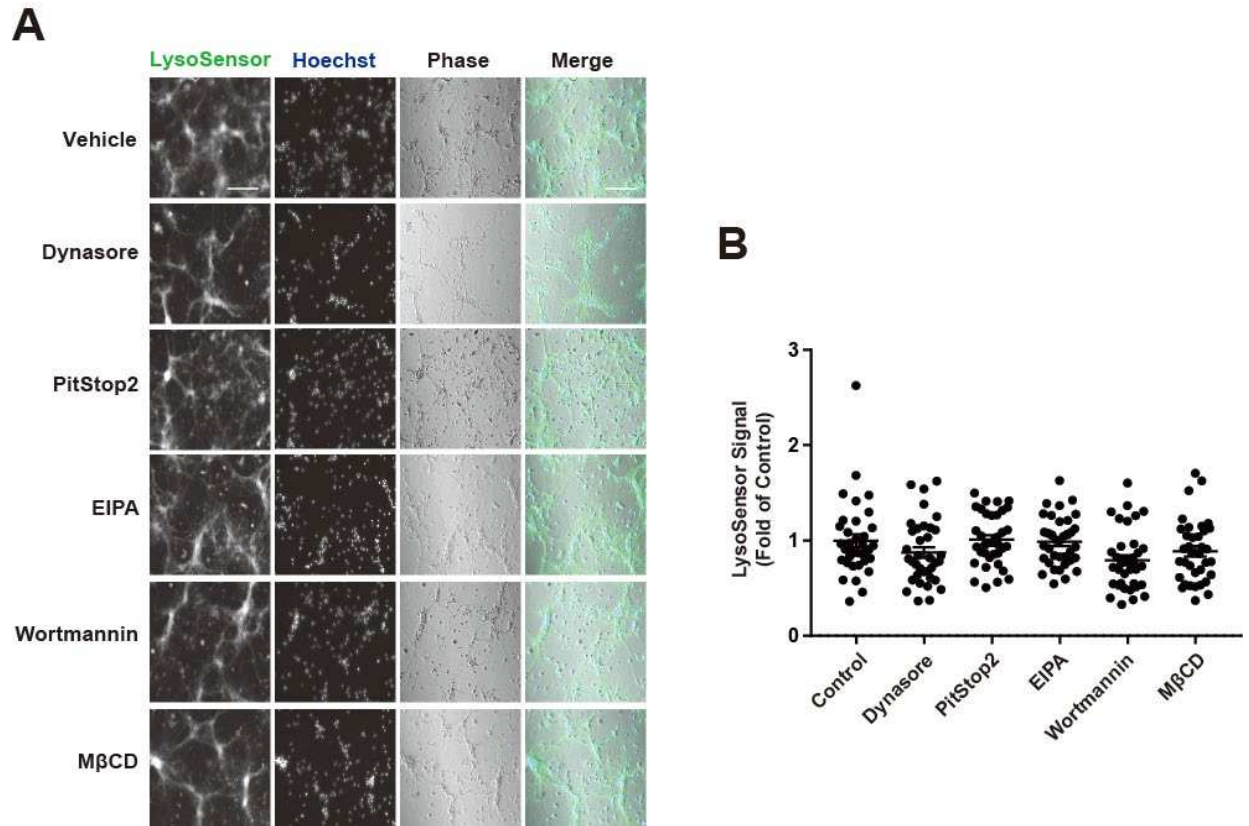


**Fig. S9. Endocytosis inhibitors in neurons do not result in acute lysosomal acidification differences within the 2-hour timeframe used here for analysis.**

- A) Widefield microscopy of primary hippocampal neurons at DIV 7, stained with 1  $\mu$ M LysoSensor (green) or Hoescht dye, shows similar neuronal morphologies and LysoSensor intensities across different conditions. Vehicle, or the indicated inhibitor, was added two hours prior to incubation with 1  $\mu$ M LysoSensor Green for 30 minutes. Cells were washed two times with Hank's Balanced Salt Solution (HBSS) before staining with Hoescht dye. Scale bar, 200  $\mu$ m.
- B) Quantification of relative LysoSensor green (i.e., lysosomal acidity) calculated as a fold-change from DMSO-only (control) treated cells. Twenty-seven images from three independent experiments were quantified for each condition, with each dot representing results from one image. Bars show group means (SEM), and one-way ANOVA analysis was not significant.

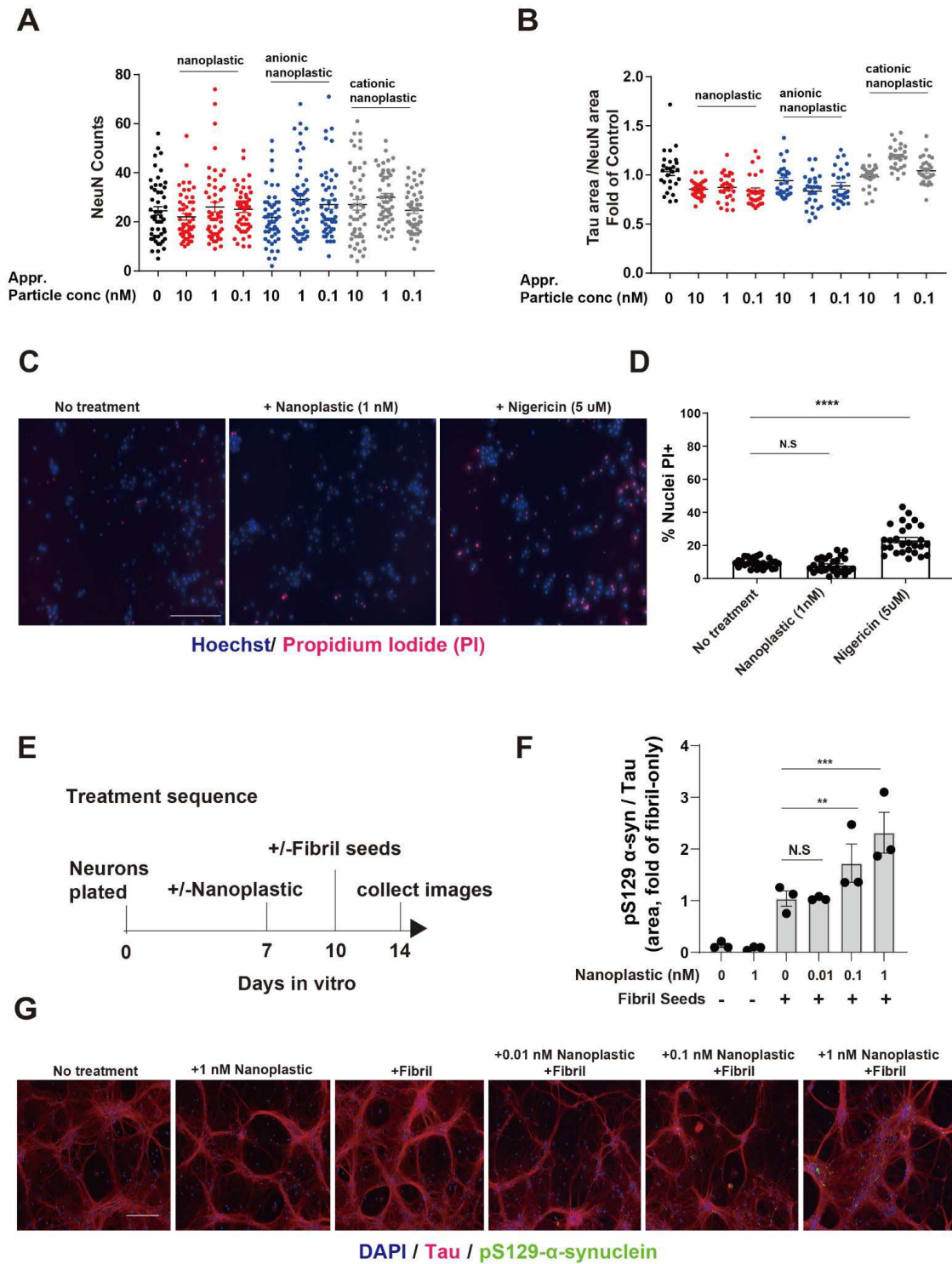


**Fig. S10. Low neuronal toxicity associated with nanoplastic exposures to primary neurons, and effects of different nanoplastic concentrations on fibril-seeded  $\alpha$ -synuclein aggregation.**

- A) Primary hippocampal neurons (DIV 7) were treated with the indicated concentration of nanoplastic particles, and column plots show image field counts for the number of NeuN-positive cells. The average number of NeuN-positive cells per field is quantified from fifty images collected from three independent experiments, where each dot represents the analysis of one image.
- B) Relative ratios of tau-positive areas to NeuN are calculated as a measure of neuronal process complexity. Each dot shows the analysis of one image of twenty-seven images from three independent experiments. Black bars are group means (SEM) in graphs in A) and B). There were no apparent losses of NeuN positivity of tau complexity with the nanoplastic concentrations indicated.
- C) Representative fluorescence from neurons exposed to 1nM of anionic nanoplastic, or neurons treated with 5  $\mu$ M nigericin for 2 hrs (an NLRP3 activator and mild neurotoxin), prior to staining with propidium iodide and Hoescht.
- D) The percentage of Hoechst nuclei that are co-positive for propidium iodide are evaluated as a measure of cell death in neurons after treatment with nanoplastic or nigericin. Dots are the mean values from each image of 27 images collected from 3 independent experiments. Black bars show group means (SEM), with significance assessed by one-way ANOVA with Tukey's post hoc test. \*\*\*\* $p < 0.0001$ , and n.s. is not significant.
- E) Graphical timeline for the sequential addition of nanoplastic (or vehicle control, at DIV 7) and then  $\alpha$ -synuclein fibrils (at DIV 10), with neurons immunostained and imaged at DIV 14.
- F) Quantification of pS129- $\alpha$ -synuclein area occupying tau-positive area as a measure of the abundance of  $\alpha$ -synuclein pathology. Each dot represents the combined (mean) analysis of images from an independent experiment. Black bars show group means (SEM), with significance assessed by one-way ANOVA with Tukey's post hoc test. \*\* $p < 0.01$ , \*\*\* $p < 0.001$  and n.s. is not significant.
- G) Representative images of neurons treated with nanoplastics and then  $\alpha$ -synuclein fibrils. Immunofluorescence images for tau and pS129- $\alpha$ -synuclein at DIV 14 are shown. Scale bars, 200  $\mu$ m.

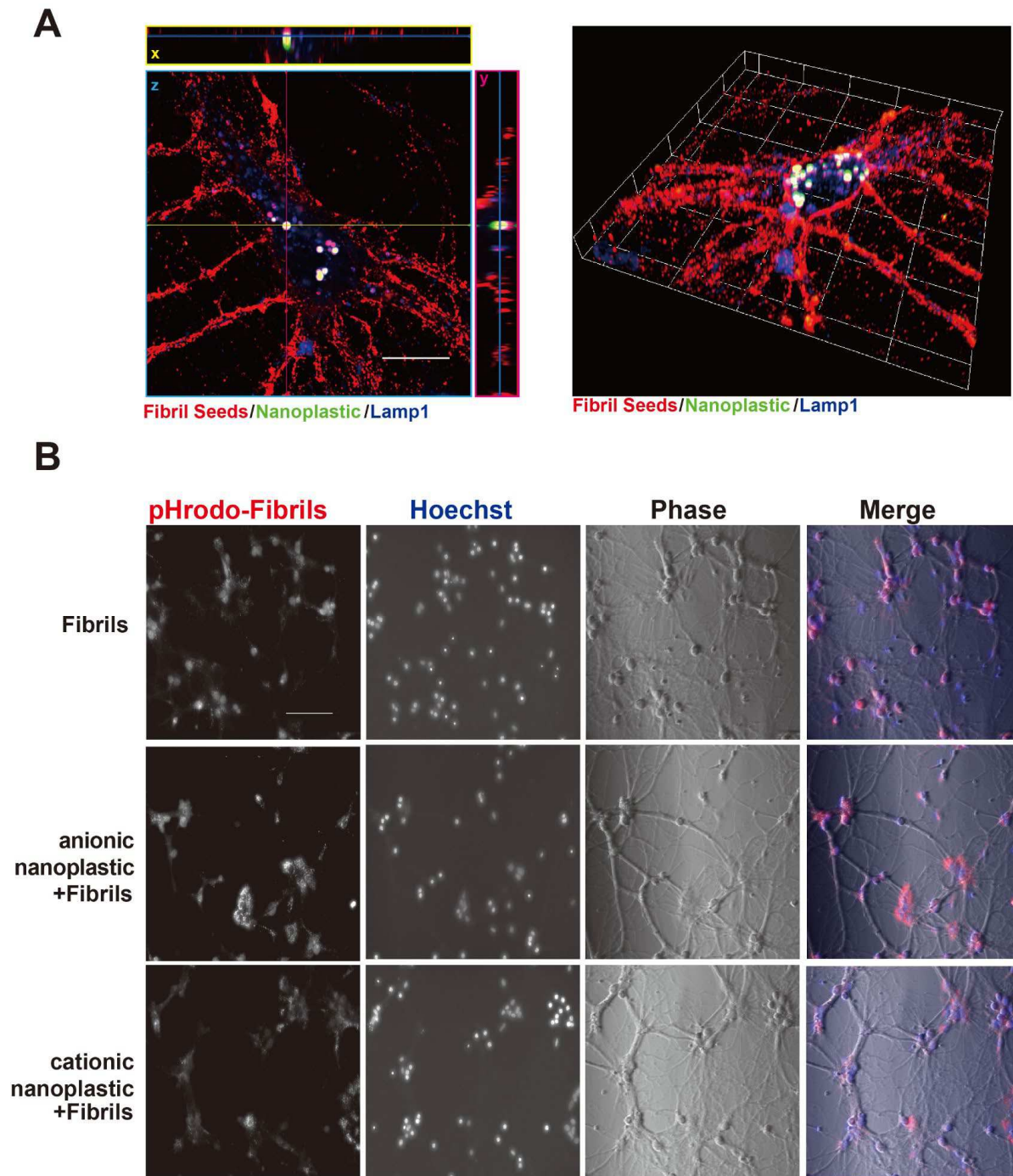


**Fig. S11. Nanoplastics do not alter the initial internalization of  $\alpha$ -synuclein fibrils into acidified vesicles in neurons.**

- A) A representative Airyscan confocal image from mouse primary hippocampal neurons (DIV 7) simultaneously exposed to both FITC-labeled nanoplastics and Alexa-647-labeled human  $\alpha$ -synuclein fibrils. Neurons were immuno-stained at 24 hours after the

addition of the particles. The orthogonal view (left panel) from sequential Z-stacks is shown. Pink line is the intersection of y,z; Yellow line is x,z; Cyan line is x,y. Cyan box is the x,y plane; Pink box is the y,z plane; Yellow box is the x,z plane. Scale bar represents 10  $\mu\text{m}$ . The reconstructed 3D view is shown in the right panel.

- B) Representative images from widefield microscopy of neurons with 1 nM of either anionic or cationic polystyrene beads added for 2 hours prior to the addition of 66.7 pM pHrodo-labeled  $\alpha$ -synuclein fibrils. Cells were washed two times with Hank's Balanced Salt Solution (HBSS) to help eliminate non-internalized particles prior to the cultures stained with Hoechst. Further, the dye pHrodo-Red should not fluoresce at all until internalized in cells into an acidified vesicle. An analysis of >50 images analyzed for each condition suggests the nanoplastic addition does not change the uptake of  $\alpha$ -synuclein fibrils into neurons. Scale bar, 200  $\mu\text{m}$

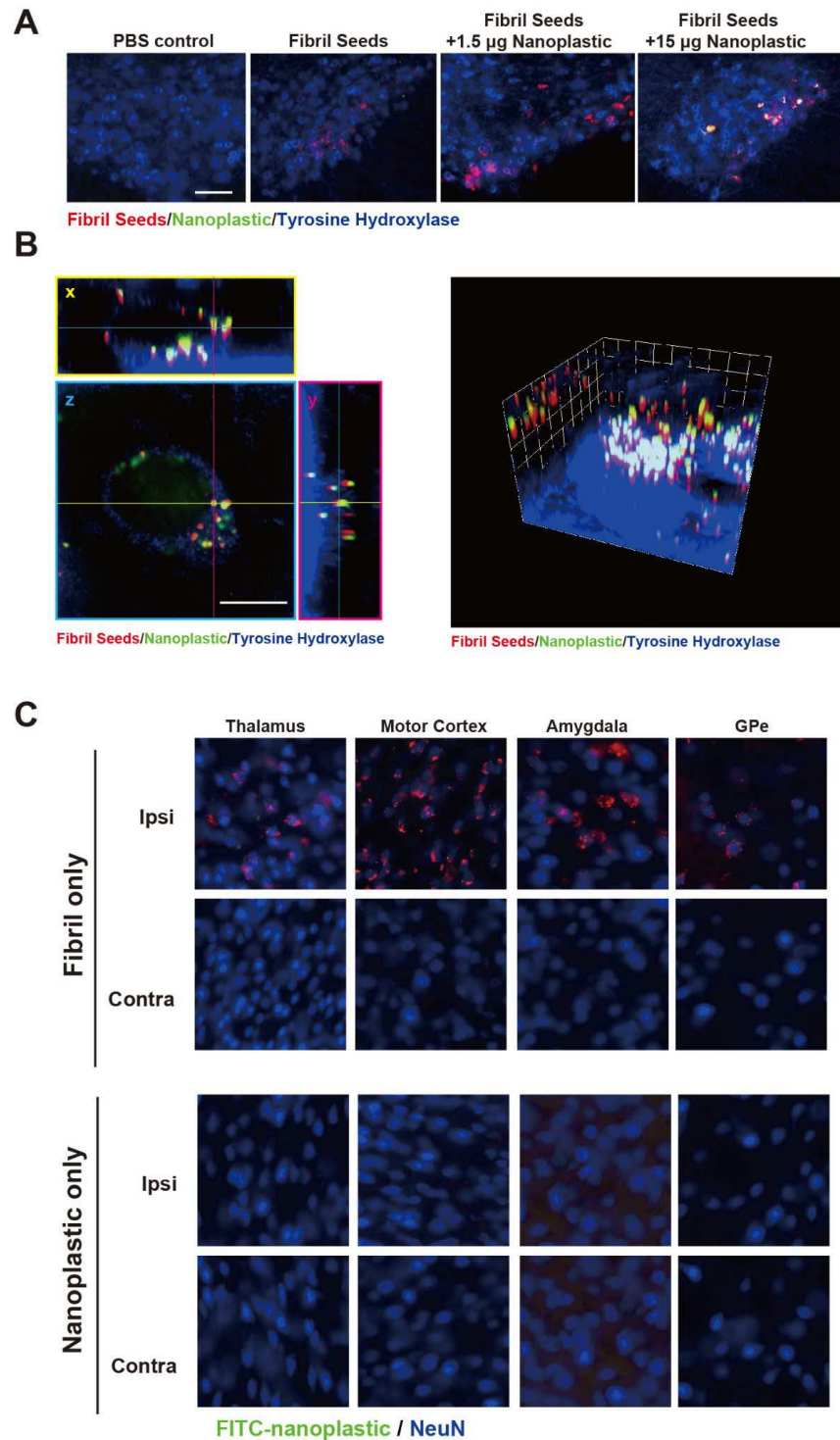


**Fig. S12. Fibril or nanoplastic spread through the mouse brain 3-days post intrastriatal injection.**

A) P90 male CD1 (non-transgenic) mice were injected unilaterally in the dorsal striatum with PBS buffer control, or 4.5  $\mu$ g Alexa-647 labeled human  $\alpha$ -synuclein fibrils, in combination with the indicated amount of FITC-conjugated nanoplastic particles. The

mouse brains were collected for analysis 3-days post-injection. Representative images of dopaminergic cells in the SNpc are shown, with fibril-only (red) or nanoplastic-only (green) injections with tyrosine hydroxylase staining (blue). Scale bar, 50  $\mu\text{m}$ .

- B) Orthogonal view (left panel) from sequential Z-stacks is shown from a dopaminergic neuron in the SNpc. Pink line is the intersection of y,z; Yellow line is x,z; Cyan line is x,y. Cyan box is the x,y plane; Pink box is the y,z plane; Yellow box is the x,z plane. Scale bar represents 10  $\mu\text{m}$ . The reconstructed 3D view is shown in the right panel.
- C) Additional representative images in the indicated brain region in mice injected with either nanoplastic particles alone or fibril particles alone. Efficient retrograde (or anterograde) spread of FITC-conjugated anionic nanoplastics (green) was not observed in contrast to labeled fibrils. Images are representative of the brain regions from six injected mice that were analyzed. Scale bar, 50  $\mu\text{m}$ .



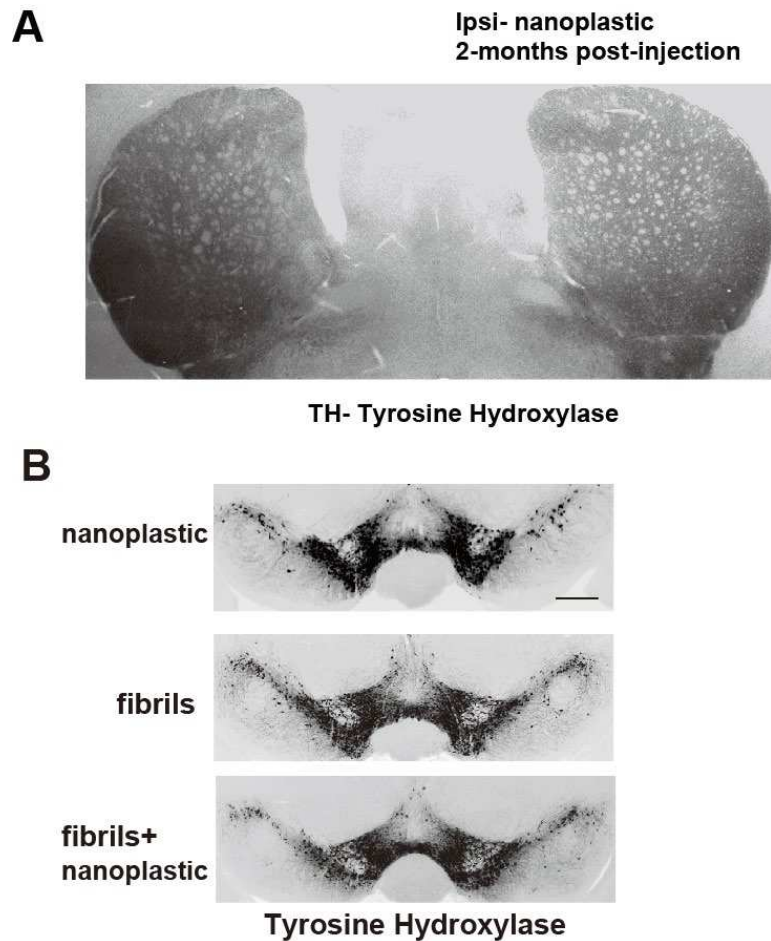


**Fig. S13. Striatal nanoplastic or human  $\alpha$ -synuclein fibril injections do not result in loss of dopaminergic neurons 2-months post injection.**

- A) Representative image of fluorescence microscopy of tyrosine-hydroxylase (TH)-stained (grayscale) dorsal striatum. Shown is a representative coronal section near the (coronal) plane of particle injection of an adult mouse 2-months post-nanoplastic injection. No obvious changes in TH+ fiber density were observed, suggesting intact nigrostriatal projections months following nanoplastic injection.
- B) Representative images of fluorescence microscopy of tyrosine-hydroxylase (TH)-stained (grayscale) substantia nigra pars compacta (SNpc). striatum. Shown is a representative coronal section near the plane of injection of an adult mouse 2-months post-nanoplastic injection. No obvious changes in the SNpc were observed in TH+ cell distribution and density, suggesting preservation of these neurons (i.e., minimal or no neuronal loss) months following nanoplastic injection, or nanoplastic with fibril injections. Scale bar, 500  $\mu$ m.

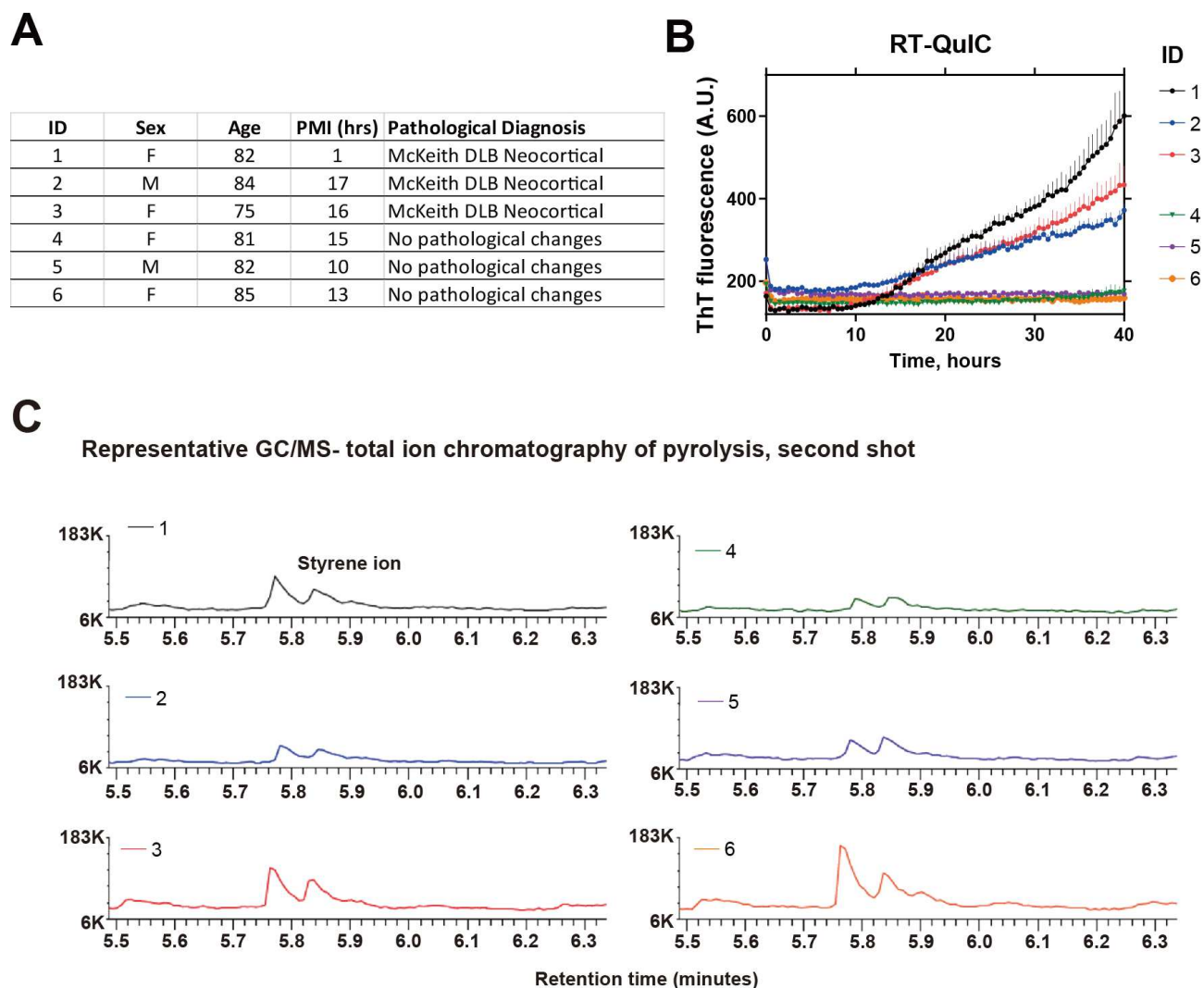


**Fig. S14. Detection of styrene ions from frontal cortex brain tissue in Lewy body disease and healthy control brain tissue samples via a double-shot pyrolysis-gas chromatography / mass spectrometry analysis.**

- Six frozen frontal-cortex brain samples were procured from the Bryan Brain Bank at Duke University that correspond to a pathological diagnosis of neocortical dementia with Lewy bodies or neurologically normal. Sex, age at death, post-mortem interval for freezing the brain samples, and pathological diagnosis are indicated.
- Results from an  $\alpha$ -synuclein seeding assay (real time quaking-induced conversion, RT-QuIC) from the frozen frontal-cortex brain tissue piece. These six brain samples were previously analyzed as part of a larger RT-QuIC-based characterization of brains from the Bryan Brain bank as previously reported (24).
- Representative ion chromatogram traces (from duplicate runs) from the analysis of 200 micrograms of desorbed (250°C, 5 min) lyophilized brain tissue fine-powder (blood vessels removed) from the indicated sample. The desorbed product elucidates semi-volatile analytes, whereas the pyrolysis step generates pyrolyzates otherwise stable to

600°C (e.g., polystyrene). A zoomed retention time for the pyrolyzates is shown highlighting peaks associated with styrene ions. All six brain samples were positive for styrene ions. Methods used for this analysis were based on a previous method of the analysis of whole blood samples from healthy controls for the presence of polystyrene nano- and microplastic polystyrene detection (8). More details for this method can be found in Supplementary Methods.

**Table S1. Source and types of nanoplastics used**

Catalog #*	Average diameter- nm (SEM)**	Charge and modification***	Fig.#
PST25C	23.2 (3.9)	Anionic (-COOH)	Fig.1C-H, Fig.3B-D, Fig.5E-H, Fig.6C-K, Fig.7A-E, Fig.9, Fig.S1A, Fig.S6D,F,H, Fig. S7, Fig.S10A-G, Fig.S11C, Fig.S13
PST50C	39.5 (0.7)	Anionic (-COOH)	Fig.1A-B
PST25A	23.5 (1.9)	Cationic (-NH <sub>2</sub> )	Fig.3B, Fig.S6E-H, Fig.S10D-E, Fig.S11C
FGP25C	36.6 (0.6)	Anionic (-COOH), FITC	Fig. 4A-B, Fig.5A-C, Fig.6A-B, Fig.7D, Fig.8, Fig.S8, Fig.S11A, Fig.S12
PST25A	29.6 (1.2)	Cationic (-NH <sub>2</sub> ), pHrodo	Fig.4C-F
PST50A	53.8 (2.8)	Cationic (-NH <sub>2</sub> ), pHrodo	Fig.4C-F
PST100A	111.9 (2.1)	Cationic (-NH <sub>2</sub> ), pHrodo	Fig.4C-F
Homemade, see methods	115.6 (34.3)	N/A	Fig.S2

\* Nanoplastic particles were purchased from Lab261, Inc.

\*\* S.E.M.s are calculated from at least triplicate independent measures using dynamic light scattering.

\*\*\*Free dyes were removed from the preparations with desalting columns prior to usage. All concentrated nanoplastics were maintained in 0.1% tween-20 to prevent aggregation of the particles prior to usage in experiments.

## Supplementary Methods

### Pyrolysis Gas Chromatography and Mass Spectrometry

Frozen frontal cortex brain samples were lyophilized overnight under vacuum. Blood vessels exhibited a leathery texture and were separated easily prior to crushing the remaining tissue into a powder. Approximately 200  $\mu\text{g}$  of the prepared powder for each sample was analyzed through loading the powder to a pyrolysis cup in a first desorption step at 250°C for 5 min to elucidate semi-volatile analytes (e.g., proteins, sugars, lipids), and a pyrolysis step at 600°C to generate pyrolyzates indicative of possible polymer(s) or ions from other heat resistant molecules. All samples were measured in duplicate with similar ion traces obtained. Resulting fragments and rearrangements were analyzed and identified by gas chromatography followed by mass spectrometry, and searched against the NIST 14 Mass Spectral Library and internal reference spectra. Desorb analysis of the samples detected high quantities of cholesterol, and lesser concentrations of other sterols, lipid fragments, and other solvents. A 10  $\mu\text{g}$  polystyrene standard was also analyzed separately to provide signal to noise data for detection limit and rough estimation of polystyrene sensitivities during the pyrolysis step. Typical reproducibility as determined by statistical process control of the measurement system is estimated at about 20% (at 95% confidence level,  $k\sim 2$ ).

## **Captions for Auxiliary Supplemental Materials**

### **Auxiliary Raw Data for “Anionic Nanoplastic Contaminants Promote Parkinson’s Disease-Associated $\alpha$ -Synuclein Aggregation.”**

Seventeen tabs, labeled corresponding to the labeled figure panels, provide all raw data used to create the graphs presented in the Figures.